# BHUTAN HydroMet *Journal*

Volume IV


National Centre for Hydrology and Meteorology
Royal Government of Bhutan
Thimphu: Bhutan

June 2026

Published by National Centre for Hydrology and Meteorology



Address: Doeboom Lam, Thimphu: Bhutan

P.O. Box No: 207

Website: www.nchm.gov.bt

Tel. No.: +975-2-327202

Fax No.: +975-2-327202

**Editorial Note**

The Bhutan HydroMet Journal continues to serve as a platform for disseminating scientific knowledge and promoting research in the fields of hydrology, meteorology, climatology, aviation meteorology, and cryosphere studies in Bhutan. Since its inception in 2022, the journal has contributed to strengthening evidence-based decision-making by publishing research that addresses emerging hydro-meteorological challenges and supports national development priorities. The Editorial Team is pleased to present the fourth volume of the journal, featuring two scientific papers that examine important aspects of climate change in Bhutan. The first paper, Interpreting Annual Mass-Balance Variability on Gangju La and Thana Glaciers in the Bhutan Himalaya Using ERA5 -Land melt and snowfall diagnostics, and the second paper, Climate Warming Impacts on Aircraft Takeoff Performance at a High-Elevation, Runway-Limited Airport: Paro International Airport. We hope that through this journal the scientific communities, students, decision makers, planners and general public will be greatly benefitted. The editorial team extends its sincere appreciation to the authors for their dedication and valuable contributions to this volume. We also acknowledge the reviewers for their constructive comments and the management of NCHM for its continued guidance and support in the publication of the journal. As the Bhutan HydroMet Journal continues to evolve, we remain committed to enhancing its scientific quality, editorial standards, and relevance. We hope that the next volume (Bhutan HydroMet Journal, Volume V) will have more Scientific articles and we would like to assure that the team will work together towards enhancing the journal.

Karma Toeb
Chief Editorial

**CONTENT** **Page**

**Interpreting Annual mass-balance variability on Gangju La and Thana Glaciers in the Bhutan Himalaya using ERA5-Land melt and snowfall diagnostics**

*Tshewang Jamtsho and Karma, Cryosphere Services Division, National Centre for Hydrology and Meteorology,*
*Correspondence:* [*karma@nchm.gov.bt*](mailto:karma@nchm.gov.bt); [tjamtsho@nchm.gov.bt](mailto:tjamtsho@nchm.gov.bt)

**Abstract**

Daily ERA5-Land reanalysis data were used to interpret short-period glacier mass-balance variability at Thana during 2023–2025 and Gangju La during 2024–2025. Positive degree days (PDD) were calculated from daily mean 2 m air temperature as indicators of melt opportunity. Potential late-spring snow buffering was assessed from April–May snowfall amount, snow fraction and the cumulative PDD occurring after each snowfall event to 31 May (postPDD→Jun1). These variables were combined in a persistence-weighted snowfall index (PWI), which assigns greater weight to snowfall events followed by limited pre-monsoon thermal exposure.

At Thana, the PWI ranking from k=20 °C day onward was consistent with the reported mass-balance point estimates: 2024 had the lowest PWI and the most negative balance, 2023 occupied an intermediate position, and 2025 had the highest PWI and the least negative balance. At Gangju La, PWI remained low at small and moderate k values, while duration-normalized PDD indicators were higher in 2024, the year with the more negative mass balance. These results demonstrate the value of combining melt-opportunity and snowfall-timing diagnostics. However, because the analysis includes only three years at Thana and two years at Gangju La, the findings are interpreted as diagnostic consistency rather than statistically conclusive attribution.

Key words: mass balance, positive degree day (PDD), persistence weighted snowfall index (PWI)

## Introduction

Glacier mass balance is controlled by the combined effects of climatic forcing and glacier specific characteristics. Key climatic drivers include air temperature, the phase and timing of precipitation and radiative conditions. These act together with local modifiers such as glacier hypsometry, aspect and shading, presence of debris cover, wind distribution and avalanching, and ice dynamics. Among these controls, positive air temperatures and snowfall events provide practical variables for interpreting interannual glacier mass-balance variability. Snow strongly influences glacier-surface albedo. Even short-lived snowfall events can temporarily reduce melt by increasing surface reflectance and delaying exposure of darker glacier ice, whereas rapid warming after snowfall can quickly remove this buffering effect.

In data sparse mountainous region temperature index approaches commonly use the sum of positive degree days (PDD) as a proxy for melt season thermal forcing when full surface energy balance data are unavailable (Hock,2003). Braithwaite and Hughes (2022) also noted that melt at the snowline relates closely to the cumulative sum of positive temperatures and that mean summer temperature can serve as an approximate proportional proxy.

Across Bhutan and in wider Hindu Kush Himalaya region studies show that seasonal snow cover is generally most extensive in winter but there is large interannual variability in snow extent and persistence among basins (Gurung et al,2011b). This variability is important for glacier mass balance interpretation since the same seasonal snowfall amount can have very different melt implications depending on when it occurs and how long it persists into the melt season. This highlights the need to consider not only seasonal snowfall totals but also the timing of snowfall relative to subsequent melt opportunity, particularly in regions with strong seasonal transitions.

The National Centre for Hydrology and Meteorology (NCHM) in Bhutan maintains an annual programme for reporting glacier mass balance from benchmark glaciers. These records are important, but there remains a need for simple and reproducible climate indicators that can help interpret year-to-year mass-balance differences across sites and survey periods.

This study applies ERA5-Land diagnostics to two benchmark glaciers in Bhutan: Thana during 2023–2025 and Gangju La during 2024–2025. The framework combines PDD, snowfall amount, snow fraction and April–May snowfall timing to interpret short-period mass-balance variability. Because the available direct observation windows contain only two to three years per glacier, the objective is to demonstrate a reproducible diagnostic framework rather than provide statistically robust attribution. Extension to the longer monitoring records will require consistently documented field-survey start and end dates.

## Study area and mass-balance windows

Thana Glacier is a benchmark glacier located in central Bhutan in the headwaters of the Chamkhar Chhu. It has an approximate surface area of 3.0 km² and extends from about 5,100 to 5,700 m a.s.l., centred near 28.02°N and 90.61°E (Figure 1). Thana has a mean surface slope of approximately 11° and a mean aspect of 114°, corresponding to an east-southeast-facing orientation.

Gangju La Glacier is a small benchmark glacier located in western Bhutan in the headwaters of the Pho Chhu. It has an approximate surface area of 0.3 km² and an elevation range of approximately 4,900–5,200 m a.s.l., centered near 27.94°N and 89.95°E (Figure 1). Gangju La has a mean surface slope of approximately 18° and a mean aspect of 14°, corresponding to a north-northeast-facing orientation.

Both glaciers are predominantly clean-ice systems, but they differ substantially in size, elevation range, slope, and aspect. Thana is larger, higher, and more gently sloping, whereas Gangju La is smaller, lower, and steeper. Their contrasting orientations may influence solar-radiation exposure, snowfall redistribution, melt conditions and seasonal snow persistence; however, these topographic effects were not independently evaluated in this study.

The analysis was restricted to years with clearly documented survey dates — 2023–2025 for Thana and 2024–2025 for Gangju La — so that the ERA5-Land diagnostic period matched the observed mass-balance window as closely as possible. ERA5-Land has a much coarser spatial resolution than either glacier, so extracted temperature, precipitation, and snowfall values are interpreted as internally consistent indicators of relative year-to-year climatic forcing rather than direct measurements of glacier-surface conditions.

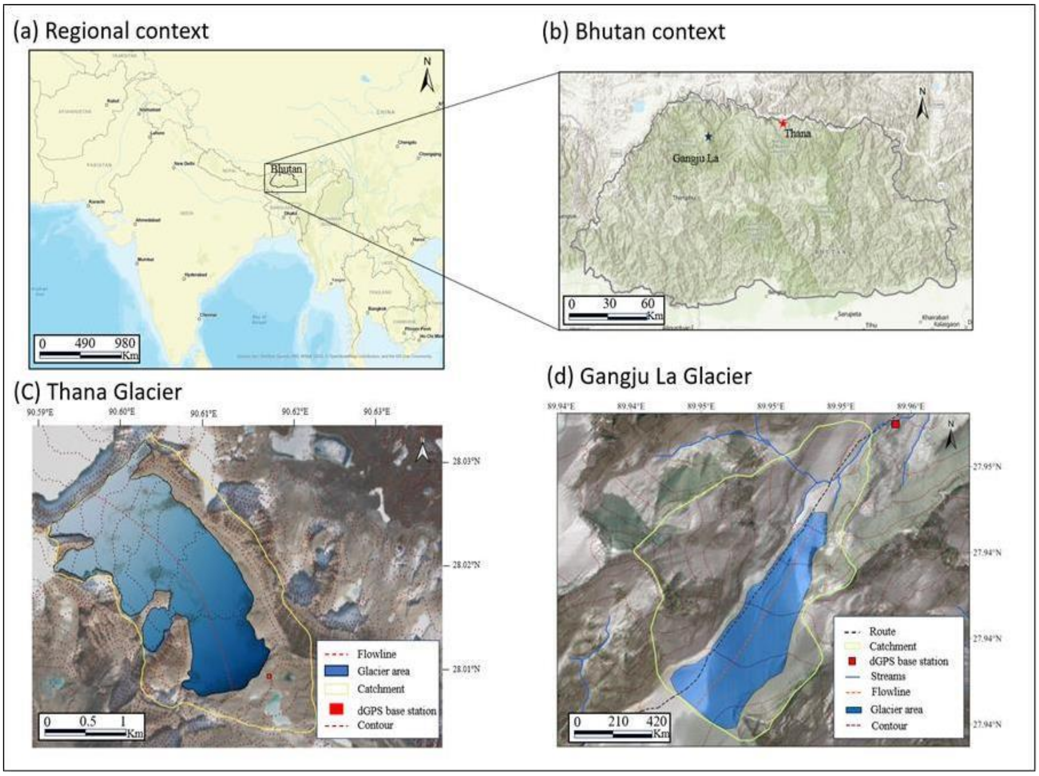


**Figure 1:** Study area showing regional and local context of Gangju La and Thana glaciers in Bhutan

## Data and methodology

ERA5-Land provides spatially continuous and internally consistent land-surface meteorological fields by combining observations with numerical-model reconstruction (Muñoz-Sabater et al., 2021). Such products are particularly useful in the Himalaya, where high-elevation observations are sparse and unevenly distributed. Previous work in Bhutan has also used ERA products to interpret unusual snowfall conditions under observational constraints (NCHM, 2025). In this study, ERA5-Land was used to derive comparative indicators of melt opportunity, snowfall occurrence and post-snow thermal exposure. It was not used to estimate exact glacier-surface energy fluxes or calibrated melt rates.

## Glacier mass-balance observations

The observed annual glacier mass-balance values and associated uncertainties for Thana and Gangju La were obtained from the benchmark glacier-monitoring technical reports and climate records of the National Centre for

Hydrology and Meteorology, Bhutan. The values used in this study were taken directly from the corresponding NCHM publications for each glacier and mass-balance year.

The present study did not independently derive or recalculate the reported mass-balance values or their uncertainties. Instead, the NCHM-reported observations were used as reference data for comparison with the ERA5-Land climatic diagnostics. The NCHM field programme includes repeated glacier-surface elevation measurements, snow and ice observations, elevation-band interpolation and glacier-wide integration. Detailed descriptions of the field procedures, density assumptions, spatial interpolation and uncertainty estimation are provided in the corresponding NCHM technical reports.

**ERA5-Land daily drivers**

Daily data were extracted from the ERA5-Land Daily Aggregated collection (ECMWF/ERA5_LAND/DAILY_AGGR). The variables used were daily mean 2m air temperature (temperature_2m), daily total precipitation (total_precipitation_sum) and daily snowfall water equivalent (snowfall_sum). Data were extracted from the nearest ERA5-Land grid cell to each glacier centroid using a fixed location for all analyzed years

**Unit conversions and derived variables**

Daily mean temperature was converted from Kelvin to degrees Celsius. Precipitation and snowfall sums were provided in metres of water equivalent and converted to millimetres. Water equivalent is abbreviated as w.e. throughout the manuscript. Daily rainfall was estimated as total precipitation minus daily snowfall, so that precipitation represents the total water input (rain + snow), while snowfall represents the solid-phase component only.

**Positive degree days**

Daily PDD was computed from the daily-mean temperature as PDD_day = max (0, T2m_C) with units of °C·day. PDD totals were the sum of daily PDD across the mass-balance period, and PDD/day was the daily mean for that period. In this study, PDD was used as a physically grounded diagnostic indicator of melt opportunity for interannual comparison, rather than as a calibrated melt estimate.

**Snow buffering metrics: snowfall totals and snow fraction**

The presence of snow on the surface of a glacier determines the nature of the melting process of the glacier, therefore it has a strong impact on the mass balance of that particular glacier. Snow buffering was quantified using snowfall totals (mm w.e) and snowfall fraction of the precipitation was defined as snowfall_total/precipitation_total. Snow fraction was used as an indicator of phase partitioning; higher snow fraction implies more precipitation falling as snow, supporting snow cover persistence and higher albedo whereas lower snow fraction implies more rain which does not increase surface albedo enhancing melt through more heat absorption and wetting. This metrics were used as supplementary diagnostics to support the interpretation that April-May snowfall timing can be more influential for subsequent ablation than total snowfall accumulated over the full mass-balance period.

**Seasonal partitioning within each mass-balance window**

Each mass-balance window was partitioned into Oct–Mar, Apr–May, and Jun–Sep based on the seasonal structure evident in the monthly ERA5-Land snowfall (events >1 mm w.e.) and precipitation series. The snow diagnostics indicated that the bulk of snowfall was delivered from October through late spring, reflecting a cold-season regime spanning the post-monsoon transition and winter (Oct–Mar), when high-elevation snowfall is commonly associated with mid-latitude westerly disturbances (typically strongest in Dec–Mar). In contrast, after May the hydroclimate shifts toward the summer monsoon (Jun–Sep), during which total precipitation increases sharply while snowfall becomes limited or episodic, implying a greater likelihood of rain-dominant precipitation under warmer conditions.

Although high-elevation meteorological observations in High Mountain Asia are sparse and uneven and no single precipitation product is universally optimal in complex terrain (Sun et al., 2021), ERA5-Land snowfall related drivers were used here as internally consistent diagnostic proxies to evaluate seasonal timing and interannual variability over each glacier, rather than as point-accurate accumulation totals. Specifically, data were extracted at the glacier centroid (nearest ERA5-Land grid cell) to provide a fixed, repeatable reference time series; these values are therefore interpreted as relative indicators of the timing and strength of snow delivery that may help explain year-to-year differences in observed glacier mass balance. Evaluations over High Mountain Asia show that

ERA5 precipitation can exhibit systematic biases (including overestimation), yet it generally captures the seasonal cycle and the broad spatial distribution and trends, supporting its utility for diagnosing climatic variability in data-scarce upstream regions (Sun et al., 2021) This diagnostic use is also consistent with Bhutan Himalayan applications in which ERA5/ERA5-Land are used to interpret snowfall events under observational constraints (NCHM, 2025, Bhutan Hydro-met Journal). Complementing these snowfall proxies, PDD derived from temperature provides a comparatively robust indicator of seasonal melt opportunity; therefore, Jun-Sep was treated as the peak melt-forcing season. Within this seasonal progression, Apr-May was treated as a dedicated shoulder-season window because it represents the final period of substantial snowfall delivery immediately preceding monsoon onset and thus most directly constrains the glacier surface state entering the monsoon (snow cover and albedo). Interannual differences in Apr-May snowfall and snow fraction are therefore expected to have a disproportionate influence on subsequent ablation by helping snow cover last longer, keeping albedo high, and delaying exposure of bare ice into early summer. This seasonal framing is consistent with the Himalayan structure of westerly-dominated cold-season precipitation and monsoon precipitation separated by a transitional shoulder season (Bookhagen & Burbank, 2010).

### Event-timing diagnostic: post-snow PDD to monsoon onset

To explicitly account for timing, an event-scale melt-exposure diagnostic was computed for each snowfall event (snowfall_sum > 1 mm w.e.) occurred during the shoulder season (April-May). Event timing diagnostic was focused on April-May of each year considering that final substantial snowfall preceding monsoon season onset occurs during this month. Post snow falls positive degree day till onset of melting season.i.e 1st June (postPDD→Jun1) was quantified using cumulative pre-monsoon melt exposure by summing daily positive degree days (PDD_day) from the day after the event to 31 May, i.e., up to but excluding monsoon onset (defined here as 1 June) as shown in equation 1. Low values indicate limited post-snow melt opportunity and therefore a higher likelihood that snowfall persists long enough to maintain higher albedo and delay exposure of low-albedo ice/debris surfaces; high values indicate rapid post-event melt exposure and short-lived snow buffering.

The onset of the monsoon season was defined as 1 June, consistent with the State of Climate report 2024 (NCHM, 2025), which identifies June–September as the primary monsoon period across the country.

$$postPDD_{\rightarrow Jun1,i} = \sum_{d=i+1}^{D_{mon}-1} PDD_{day(d)}, D_{mon} = 1\,June \tag{1}$$

**Persistence-weighted snowfall to monsoon onset (PWI) and k-sensitivity**

A persistence-weighted snowfall index (PWI) was defined for the Apr-May window to combine snowfall amount with its likelihood of persisting into monsoon-onset melt conditions. PWI was defined using the following equation:

$$PWI(k) = \sum_{i=1}^{N} S_i \exp\left(-\frac{postPDD_{\rightarrow Jun1,i}}{k}\right) \tag{2}$$

Where $S_i$ is snowfall (mm w.e.) for event $i$, and $postPDD_{\rightarrow Jun1,\, i}$ is as estimated using equation (1), k (°C·day) is a persistence scale that controls how rapidly a snowfall event is down-weighted as pre-monsoon melt opportunity accumulates between snowfall and monsoon onset. In this formulation, PWI represents effective (timing-weighted) snowfall for Apr–May: events followed by large postPDD→Jun1 receive low weight and contribute little to buffering, whereas events with low postPDD→Jun1 retain high weight and contribute strongly to buffering. This exponential weighting was as an adapted empirical diagnostic inspired by Brock-type snow-ageing formulations, in which snow properties decay with accumulated thermal exposure since snowfall, and by the broader positive-degree-day framework commonly used in snow and glacier melt studies. PWI represents timing-weighted April–May snowfall under the assumed decay function. It is interpreted as a comparative indicator of potential snow buffering and not as a measurement of retained snow, observed snow-cover duration or a standalone predictor of annual glacier mass balance.

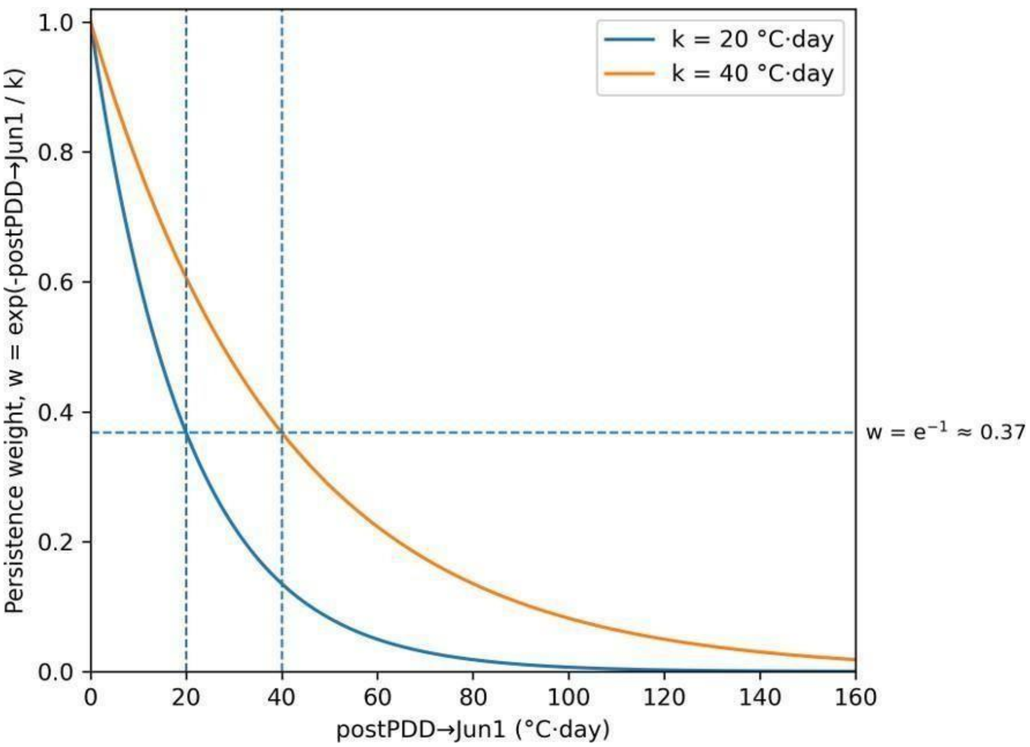


**Figure 2:** Exponential persistence weight used in the persistence-weighted snowfall index (PWI). The dashed line marks w = e−1 ≈ 0.37, which occurs when postPDD→Jun1 = k. Smaller k down-weights snowfall more rapidly with increasing pre-monsoon melt opportunity; larger k retains more weight under the same postPDD→Jun1.

## Choice of k and sensitivity analysis

An exponential melt-exposure factor was applied as $W = \exp\left(-\frac{\text{postPDD}_{\rightarrow\text{Jun1},i}}{k}\right)$ where postPDD-$_{\text{jun1}}$ is the cumulative positive degree-day exposure following each snowfall event to 31 May, as defined in Equation (1). The principal value $k$ = 20 °C·day was guided by the Brock-type snow-albedo ageing formulation implemented for the Langtang catchment by Stigter et al. (2017). In that formulation, shallow-snow albedo decreases exponentially with accumulated positive daily maximum temperature according to $w = \exp(-a_3P)$, where $P$ is accumulated positive-temperature exposure and $a_3$ is the exponential decay coefficient. Stigter et al. (2017) used $a_3$= 0.058 (°C·day)$^{-1}$.

The exponential expression used in the present study, $w = \exp(-P/k)$, has the same mathematical form as the Langtang decay expression, $w = \exp(-a_3P)$. The two exponents can therefore be equated as $a_3P = P/k$. Cancelling $P$ from both sides gives $a_3 = 1/k$, or equivalently $k = 1/a_3$. Using $a_3 = 0.058$ gives $k = 1/0.058 \approx 17.2$ °C·day. This value was rounded to $k$ = 20 °C·day to avoid implying excessive precision in an event-based diagnostic derived from reanalysis data.

The parameter $k$ represents an e-folding thermal scale. When postPDD = $k$, the weight becomes $w = \exp(-1) = e^{-1} \approx 0.37$. Thus, a snowfall event retains approximately 37% of its initial weight after experiencing accumulated positive-temperature exposure equal to the selected persistence scale.

The Langtang formulation provides an empirical and physically informed basis for the exponential decay structure. However, $k$ = 20 °C·day was not calibrated specifically for Thana or Gangju La. The Langtang formulation used accumulated positive daily maximum temperature to represent snow-albedo ageing, whereas the present study uses post-snow PDD derived from daily mean 2 m air temperature as an indicator of melt opportunity. Therefore, $k$ = 20 °C·day is treated as an adapted reference scale rather than a locally measured snow-persistence constant.

To assess whether the interpretation depended on the selected persistence scale, PWI was calculated using $k$ = 5, 10, 20, 40, 60 and 80 °C·day. Smaller values of $k$ represent more rapid assumed decay of snowfall influence, whereas larger values represent slower decay. The purpose of the sensitivity analysis was not to identify a universally correct value of $k$, but to determine whether the relative ordering of years and the contrast between Thana and Gangju La remained consistent under different persistence assumptions.

As an additional summary of sensitivity, the ratio R was calculated:

$$R = PWI40 / PWI20. \qquad (3)$$

PWI20 represents the reference case using $k$ = 20 °C·day, while PWI40 represents the slower-decay case using $k$ = 40 °C·day. A value of $R$ close to 1 indicates that increasing $k$ from 20 to 40 produces relatively little change in PWI, whereas a larger value indicates greater sensitivity to the assumed persistence scale. However, $R$ can become numerically large when $PWI_{20}$ is close to zero, as observed at Gangju La. The ratio is therefore treated as a supplementary indicator, while the complete PWI values across $k$ = 5–80 °C·day are used for the main sensitivity interpretation.

## Results

### Observed annual mass balance and diagnostic drivers

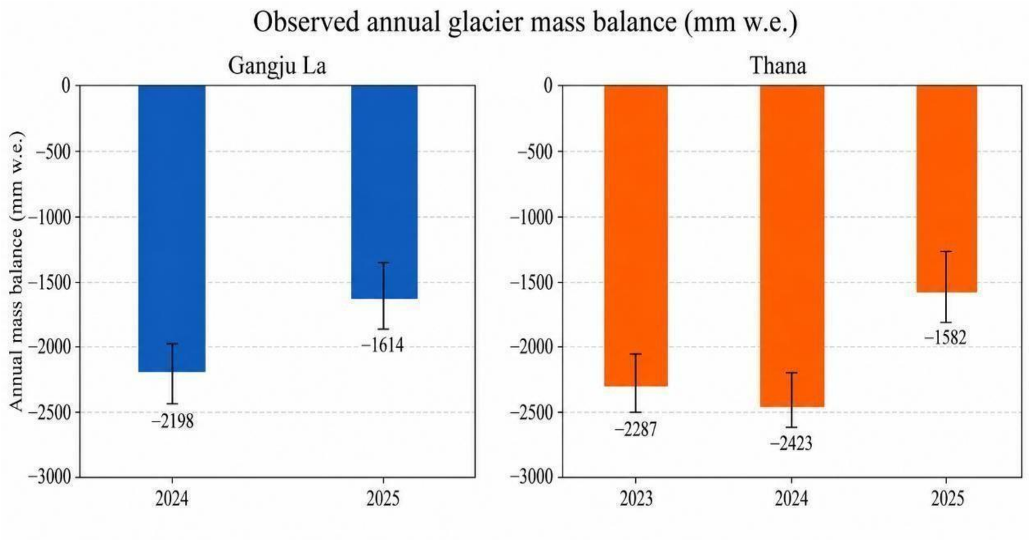


**Figure 3**. Observed annual glacier mass balance for Gangju La and Thana glacier

The observed annual mass balance of Gangju La glacier for the year 2024 & 2025 and Thana glacier for the years 2023, 2024 & 2025 reported by the NCHM benchmark monitoring programmed is presented in Table 1 and Figure 3. The study did not observe consistent mass balance trend over the observed period. However, there is significant annual variations in the estimated values.

An attempt to correlate these variations with the melt opportunity (PDD/day and melt day frequency), snowfall buffering (snowfall totals and snow fractions) and the timing of spring snowfall relative to pre monsoon melt exposure (snowfall post event PDD>Jun1 and PWI) have been made in the following section

**Table 1**. Observed annual glacier mass balance for Thana and Gangju La.

| Site | Mass-balance year | Observed annual mass balance (mm w.e.) |
|---|---|---|
| Gangju La | 2024 | -2198.4 ± 265.74 |
| Gangju La | 2025 | -1613.9 ± 236.50 |
| Thana | 2023 | -2287.4 ± 230.35 |
| Thana | 2024 | -2422.9 ± 197.04 |
| Thana | 2025 | -1581.7 ± 231.07 |

## Thana: three-window context (2023–2025)

The melt forcing (PDD/day; melt day frequency), snow buffering (snowfall, snow fraction) on Thana glacier as derived from the ERA5 data set for the three-mass balance window is presented in table 2. Similarly melt forcing and snowfall derived from the same dataset for three partitioned seasons (Oct-March, April-May, Jun-Sept) for the three-mass balance window is presented in table 3.

**Table 2.** Thana: annual ERA5-Land diagnostics for 2023–2025.

| Window | Days | PDD total (°C·day) | PDD/day (°C·day) | Melt days (%) | Snow total (mm w.e.) | Rain total (mm) | Snow fraction (%) |
|---|---|---|---|---|---|---|---|
| 2023 | 367 | 409.16 | 1.11 | 34.88 | 682.17 | 711.51 | 48.95 |
| 2024 | 358 | 503.23 | 1.41 | 36.31 | 521.98 | 816.03 | 39.01 |
| 2025 | 357 | 465.39 | 1.30 | 34.17 | 582.58 | 721.91 | 44.66 |

**Table 3.** Thana: seasonal partitioning of snowfall and melt forcing (Oct–Mar, Apr–May, Jun–Sep) within each mass-balance window.

| Window | Oct–Mar snow(mm) | Oct–Mar PDD (°C·day) | Apr–May snow (mm) | Apr–May snow days (>1 mm) | Jun–Sep PDD (°C·day) | Jun–Se p rain (mm) | Jun–Sep snow (mm) |
|---|---|---|---|---|---|---|---|
| 2023 | 277.3 | 9.5 | 166.5 | 46 | 398.6 | 679.4 | 238.3 |
| 2024 | 241.4 | 7.7 | 146.1 | 42 | 479.8 | 759.5 | 134.5 |
| 2025 | 263.4 | 1.1 | 230.7 | 54 | 458.2 | 658.3 | 88.5 |

Observed annual glacier mass balance for Thana during the three windows ranged from -2422 mm w.e in 2024 (most negative) to -2287.40 mm w.e in 2023 and -1581.7 mm w.e in 2025 (Tab. 1).

Indicators of melt intensity show that glacier melt was strongest in 2024 with the highest PDD/day (1.41) and the largest proportion of melt days (36.31%). Melt conditions were weakest in 2023 (PDD/day =1.11; melt days = 34.88%), while 2025 showed intermediate values (PDD/day =1.30; melt days=34.17%) (Table 2; Figure 4).

Snow related variables indicate that 2023 had the highest snow fraction (48.95%) and the greatest total snowfall (682.17 mm w.e), whereas 2024 recorded the lowest snow fraction (39.01%) and the lowest total snowfall (521.98 mm w.e) (Tab. 2).

Snow related variables indicate that 2023 had the highest snow fraction (48.95%) and the greatest total snowfall (682.17 mm w.e), whereas 2024 recorded the lowest snow fraction (39.01%) and the lowest total snowfall (521.98 mm w.e) (Tab. 2).

Seasonal analysis shows that the June-September period contributed most to annual PDD totals (398.6-479.8 °C·day) with the highest June - September PDD observed in 2024 (479.8°C·day). In contrast, April - May snowfall was greatest in 2025 (230.7 mm across 54 events >1 mm), compared with 2023 (166.5 mm; 46 events) (Tab. 3).

Monthly snowfall events (>1 mm w.e) show a clear cold season pattern, occurring mainly from October to May. During the peak monsoon months, particularly July and August, snowfall is limited and occurs only occasionally. However, snowfall can occur during the early monsoon (June) and the late monsoon or transition period (September). Spring snowfall in April - May varies between years with higher late season snowfall in 2025 compared to 2023 and 2024. In contrast total monthly precipitation reaches its maximum during June-September (Fig. 4),

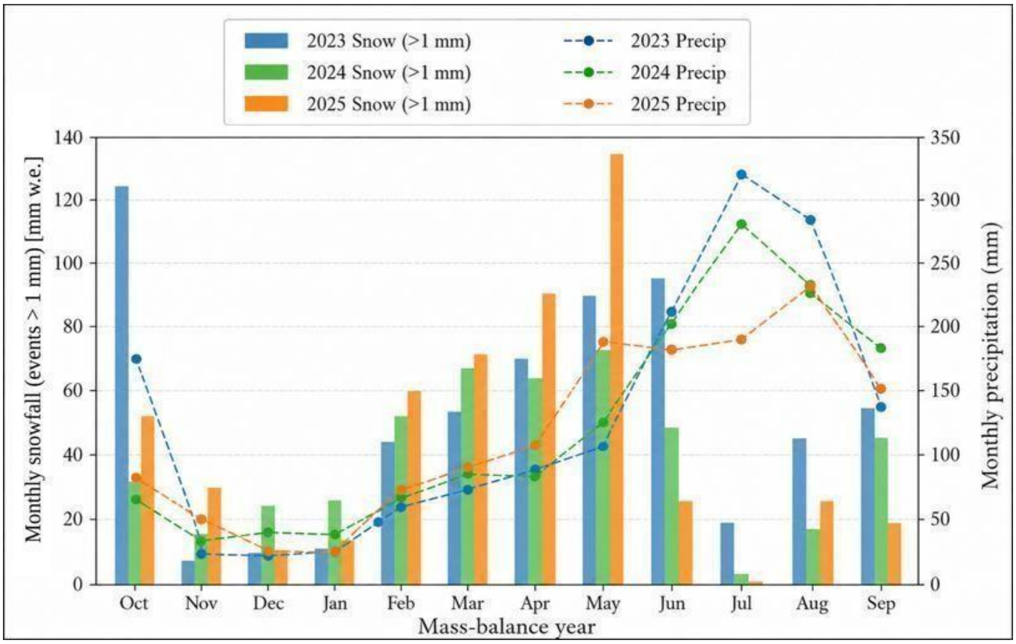


**Figure 4:** Thana: Monthly snowfall (bars; events > 1 mm w.e.) and monthly precipitation for mass-balance years 2023–2025.

## Gangju La: two-window context (2024–2025)

Melt forcing factors for Gangju La Glacier during the two mass balance periods (2024 and 2025), derived from the ERA5 dataset, are presented in Table 4 and Figure 5.Seasonally partitioned melt forcing values, calculated from the same ERA5 dataset, are shown (Tab 5, Fig. 5).

**Table 4.** Gangju La: annual ERA5-Land diagnostics for 2024–2025.

| Window | Days | PDD total (°C·day) | PDD/day (°C·day) | Melt days (%) | Snow total (mm w.e.) | Rain total (mm) | Snow fraction (%) |
|---|---|---|---|---|---|---|---|
| 2024 | 427 | 1405.64 | 3.29 | 59.48 | 462.83 | 2389.04 | 16.23 |
| 2025 | 286 | 804.24 | 2.81 | 54.20 | 331.27 | 1501.16 | 18.08 |

For Gangju La glacier, the reported glacier mass balance was -2198.36 mm w.e in 2024 and-1613.88 mm w.e in 2025 (Tab.1). The 2024 survey lasted 427 days while the 2025 survey lasted286 days (Tab. 4). Total positive degree days (PDD) were higher in 2024 at 1405.64 C.day compared to 804.24 C.day in 2025. Total PDD was greater during the longer 2024 survey window, but direct comparison of totals is affected by the unequal window lengths.

When adjusted for survey duration, melt indicators remained higher in 2024 with PDD/day of 3.29 and 59.48% melt days while in 2025 PDD/day was 2.81 and 54.20% melt days (Tab. 4, Fig. 5). Snow buffering was limited in both years with low snow fraction values between 16.23% and 18.08% respectively. Total snowfall was lower in 2025 at 331.27 mm w.e than in 2024 at 462.83 mm w.e (Tab. 4).

Seasonal analysis shows that June to September contributed most of the annual PDD with 1108.5 C.day in 2024 and 635.4 C.day in 2025. Meanwhile, the snowfall from April to May was similar in both years ranging from 92.4 to 105.0 mm across 28 to 29 snowfall events greater than 1 mm w.e (Tab. 5).

Monthly snowfall events greater than 1 mm w.e were mainly concentrated during the winter and pre-monsoon periods, roughly from October to May. The highest monthly snowfall usually occurred in February and March, while snowfall was observed limited during July and August (Fig. 5). In contrast, total monthly precipitation peaked during the monsoon season from July to September, showing a clear seasonal separation between snowfall and peak monsoon rainfall.

**Table 5.** Gangju La: seasonal partitioning of snowfall and melt forcing (Oct–Mar, Apr–May, Jun–Sep) within each mass-balance window.

| Window | Oct–Mar snow (mm) | Oct–Mar PDD (°C·day) | Apr–May snow (mm) | Apr–May snow days (>1 mm) | Jun–Sep PDD (°C·day) | Jun–Sep rain (mm) | Jun–Sep snow (mm) |
|---|---|---|---|---|---|---|---|
| 2024 | 360.0 | 176.4 | 92.4 | 28 | 1108.5 | 1795.4 | 10.4 |
| 2025 | 218.1 | 33.1 | 105.0 | 29 | 635.4 | 1019.2 | 8.1 |

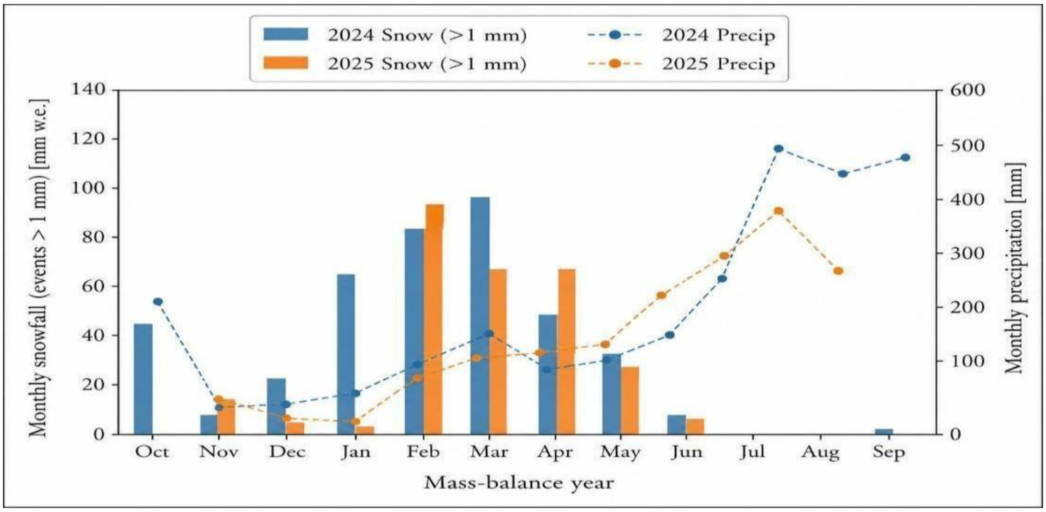

**Figure 5:** Gangju La: Monthly snowfall (bars; events > 1 mm w.e.) and monthly precipitation from ERA5-Land for mass-balance years 2024–2025.

## Event-timing diagnostic: post-snow PDD to monsoon onset (postPDD→Jun1)

Seasonal snowfall totals are not enough to determine if snowfall effectively reduces ablation. The timing of melt forcing in relation to snowfall events is crucial. The post PDD-June 1 metric measures the total positive degree days (PDD) that occur after each snowfall event until June 1. This gives an idea of the potential for melting after snowfall.

From April to May the count of snowfall events ranges from 42 to 54 at Thana glacier and from 28 to 29 at Gangju La glacier (Tab. 6). At Thana glacier the median post PDD-June 1 values are 1.08 °C.day for 2023, 15.70 °C.day for 2024, and 6.11 °C.day for 2025. In all three years 100% of events are below 40 °C·day threshold (Tab. 6).

In contrast, Gangju La glacier shows much higher median post PDD-June 1 values. These reached 107.12 °C.day in 2024 and 112.81 °C.day in 2025. Only 3.6% of the 2024 snowfall events were below both the 20 and 40 °C·day thresholds, while none of the 2025 events were below either threshold. (Tab. 6).

The clustering of postPDD-june 1 values at Thana glacier shows consistently low melt opportunity during April to May at the centroid grid cell for all years. This implies most snowfall events have low cumulative PDD before June 1 indicating good conditions for short term snow retention.

**Table 6.** Apr–May snowfall events and pre-monsoon melt exposure to monsoon onset (postPDD→Jun1).

| Site | Window | | N Apr–May events | Median event snow (mm) | Median postPDD→Jun 1 (°C·day) | P25 | P75 | % ≤20 | % ≤40 |
|---|---|---|---|---|---|---|---|---|---|
| Thana | 2023 | | 46 | 2.88 | 1.08 | 1.08 | 1.08 | 100.0 | 100.0 |
| Thana | 2024 | | 42 | 2.65 | 15.70 | 15.70 | 15.70 | 100.0 | 100.0 |
| Thana | 2025 | | 54 | 3.43 | 6.11 | 6.11 | 6.1 | 100.0 | 100.0 |
| Gangju La | 2024 | | 28 | 2.63 | 107.12 | 90.9 | 116.3 | 3.6 | 3.6 |
| Gangju La | 2025 | | 29 | 2.27 | 112.81 | 109.2 | 131.5 | 0.0 | 0.0 |

## Persistence-weighted snowfall to monsoon onset (PWI) and k-sensitivity

PWI combines Apr–May snowfall totals with melt opportunity accumulated between each snowfall event and monsoon onset (postPDD→Jun1) to provide a relative index of transition-season snowfall buffering into the monsoon. PWI is not intended as an absolute physical quantification of retained snow; rather, it is designed for interannual comparison within a site under a consistent definition of snowfall events and melt exposure. Table 7 shows PWI20 (k = 20 °C·day) with PWI40 (k = 40 °C·day) as a sensitivity bound and the ratio R = PWI40/PWI20. At Thana, PWI20 ranged from 68.55 mm w.e. (2024) to 176.65 mm w.e. (2025), with 151.16 mm w.e. in 2023, and R remained relatively close to unity (1.03–1.40). At Gangju La, PWI20 was much smaller (3.28 mm w.e. in 2024 and 0.79 mm w.e. in 2025) and k-sensitivity was larger (R = 2.67 in 2024 and 8.50 in 2025) (Tab. 7).

**Table 7.** Persistence-weighted snowfall index (PWI) for Apr–May (transition-season buffering to monsoon onset).

| Site | Window | N events | Total snow (mm w.e.) | Median postPDD→Jun 1 (°C·day) | PWI20 (mm w.e.) | PWI40 (mm w.e) | Sensitivity ratio R = PWI40/PWI 20 |
|---|---|---|---|---|---|---|---|
| Gangju La | 2024 | 28 | 81.10 | 107.12 | 3.28 | 8.77 | 2.67 |
| Gangj u La | 2025 | 29 | 95.23 | 112.81 | 0.79 | 6.73 | 8.50 |
| Thana | 2023 | 46 | 159.55 | 1.08 | 151.16 | 155.30 | 1.03 |
| Thana | 2024 | 42 | 136.52 | 15.70 | 68.55 | 96.05 | 1.40 |
| Thana | 2025 | 54 | 226.65 | 6.11 | 176.65 | 199.79 | 1.13 |

**Table 8.** Sensitivity of April-May PWI to persistence scale k. Values are in mm w.e.

| Site | Year | PWI5 | PWI10 | PWI20 | PWI40 | PWI60 | PWI80 |
|---|---|---|---|---|---|---|---|
| Thana | 2023 | 128.55 | 143.22 | 151.16 | 155.30 | 156.70 | 157.41 |
| Thana | 2024 | 15.50 | 37.10 | 68.55 | 96.05 | 107.84 | 114.33 |
| Thana | 2025 | 91.37 | 139.55 | 176.65 | 199.79 | 208.30 | 212.72 |
| Gangju La | 2024 | 2.78 | 2.78 | 3.28 | 8.77 | 16.73 | 24.17 |
| Gangju La | 2025 | 0.00 | 0.04 | 0.79 | 6.73 | 15.53 | 24.06 |

At Thana, PWI increases progressively with k in all three years but the rate of increase differs meaningfully between years. In 2023, PWI is already relatively high at k = 5 (128.55 mm w.e.) and converges toward a stable value by k = 40–60, indicating that most April–May snowfall events were followed by very low post-snow melt exposure and the buffering signal is robust across a wide range of persistence assumptions. In 2024, PWI at k = 5 is very low (15.50 mm w.e.) and rises substantially through k = 40 (96.05 mm w.e.), reflecting that a larger proportion of events experienced meaningful pre-monsoon melt exposure, making the buffering estimate more sensitive to the assumed decay rate. In 2025, PWI at k = 5 (91.37 mm w.e.) is intermediate but converges to the highest value across all Thana years by k = 40–80, consistent with moderate post-snow melt exposure but ultimately strong late-spring buffering potential. Across Thana, the ranking of years by PWI — with 2025 showing the strongest buffering potential and 2024 the weakest — is preserved across all k values from k = 20 onward, indicating that the interannual contrast is robust and not an artifact of the choice of persistence scale.

At Gangju La, PWI remains very low at small and moderate (k) values and increases mainly under larger persistence assumptions. This pattern is consistent with the high postPDD→Jun1 values shown in Table 6. Within the tested framework, April–May snowfall therefore receives limited weight unless slow decay is assumed. Because (k) has not been locally calibrated, these results are interpreted as sensitivity behaviour rather than proof of actual snow survival. PWI remains near zero for both years at small k values (k = 5: 2.78 mm w.e. in 2024; 0.00 mm w.e. in 2025), indicating that under any assumption of rapidsnow ageing, April–May snowfall contributed negligible buffering before monsoon onset. PWI values only become appreciable at k = 60–80 °C·day, which represents slower decay than is typically supported by observationalsnow-ageing studies. This implies that the near-zero buffering result at Gangju La is not sensitive to the precise choice of k within a physically reasonable range, and that the low PWI at this site reflects a genuine diagnostic signal of high post-snow melt exposure rather than methodological artifact.

## Discussion

The observed glacier mass-balance values show substantial interannual variability at both Thana and Gangju La. Interpreting these differences requires consideration of both melt opportunity and snowfall buffering. Positive degree days provide an indicator of the thermal conditions that may support melt, while snowfall amount, snow fraction and snowfall timing influence the likelihood that a bright snow-covered surface persists and delays exposure of darker glacier ice. These processes are closely linked because snowfall can temporarily reduce absorbed solar radiation through increased surface albedo, but this effect depends on the amount of snow, the timing of the event and the thermal conditions that follow it. The present analysis therefore combines PDD-based melt opportunity with the persistence-weighted snowfall index rather than treating either factor as an independent explanation of annual glacier mass balance.

Temperature-index approaches have long been used to characterize glacier melt opportunity in data-sparse mountain regions because cumulative positive temperatures are strongly related to snow and ice ablation (Hock, 2003; Braithwaite & Hughes, 2022). However, the relationship between air temperature and glacier mass balance is modified by the state of the glacier surface. A snow-covered surface has a higher albedo than exposed glacier ice and therefore absorbs less shortwave radiation. Snowfall during the transition from winter to the main melt season can consequently influence the amount and timing of subsequent ablation. Previous studies in High Mountain Asia have similarly shown that variations in snowfall amount, timing and persistence can alter glacier albedo and contribute to interannual mass-balance variability (Johnson & Rupper, 2020; Kumar et al., 2019; Ren et al., 2024). The results from Thana and Gangju La are broadly consistent with this combined temperature–snowfall framework, although the relative importance of the two diagnostic components differs between the glaciers.

At Thana, the reported mass-balance point estimates show a consistent ordering with April–May PWI from k = 20 °C·day onward. The lowest PWI occurred in 2024, which also had the most negative mass-balance point estimate. The 2023 values occupied an intermediate position for both PWI and mass balance, while 2025 had the highest PWI and the least negative balance. This consistent rank ordering is important because it indicates that the apparent relationship is not produced by a single selected persistence scale. From $k$ = 20 to 80 °C·day, the ordering of the three years remains unchanged, with 2024 showing the weakest potential buffering, 2023 an intermediate condition and 2025 the strongest potential buffering. The result therefore supports the diagnostic relevance of April–May snowfall amount and timing at Thana.

The difference between Thana 2024 and 2025 provides the clearest illustration of this pattern. The 2024 window had the highest annual PDD/day, the highest proportion of melt days, the lowest total snowfall, the lowest snow fraction and the lowest PWI among the three years. These conditions are collectively consistent with greater melt opportunity and weaker potential snow buffering. In contrast, 2025 had substantially greater April–May snowfall, a larger number of snowfall events and the highest PWI. Although June–September PDD remained relatively high in 2025, the mass balance was considerably less negative than in 2024. This suggests that thermal forcing alone does not fully describe the observed contrast. Greater late-spring snowfall and lower post-snow melt exposure may have allowed snow cover to remain effective for longer, maintaining a higher-albedo surface and delaying exposure of glacier ice during the early part of the melt season.

The 2023 Thana results strengthen this interpretation when considered within the complete three-year ordering. The 2023 PWI was lower than in 2025 but higher than in 2024 from k = 20°C·day onward, while its mass-balance point estimate was also intermediate between those years. In addition, 2023 had the highest annual snowfall total and snow fraction, but April–May snowfall was lower than in 2025. This distinction shows why whole-window snowfall totals should not be interpreted alone.A high annual snowfall total may include snow delivered during periods when it has less influence on the glacier surface entering the main melt season, whereas the PWI specifically emphasizes April–May events according to the melt opportunity following each event. The Thana comparison therefore suggests that the timing and persistence of late-spring snowfall may provide additional information beyond total snowfall and snow fraction.

Nevertheless, the Thana pattern should be interpreted cautiously as only three annual observations are available. The observed ordering is therefore a diagnostic pattern rather than statistical evidence of a relationship. It is also possible that other processes not represented in the present framework contributed to the annual differences. These include shortwave and longwave radiative forcing, wind redistribution of snow, sublimation, local shading, spatial variation in accumulation, glacier hypsometry and glacier dynamics. The PWI does not incorporate these processes directly. Its value lies in providing a reproducible indicator of one plausible mechanism—late-spring snow buffering—that can be evaluated together with other available climatic diagnostics.

At Gangju La, the climatic context differs markedly from that at Thana. Both Gangju La years had much lower annual snow fractions and substantially higher median postPDD→Jun1 values. This indicates that April–May snowfall events were followed by considerably greater pre-monsoon thermal exposure in the ERA5-Land grid cell. As a result, PWI remained low at small and moderate k values in both years. The April–May snowfall totals were relatively similar, but their weighted contributions remained limited because the subsequent PDD values were high. Within the adopted framework, this suggests weaker potential for April–May snowfall to maintain a persistent high-albedo surface before the monsoon.

The difference between the two Gangju La years is more clearly associated with melt-opportunity indicators. The 2024 survey window had higher PDD/day and a greater percentage of melt days than 2025, and it also had the more negative observed mass balance. Total PDD was also higher in 2024, although direct comparison of the totals is affected by the unequal lengths of the two survey windows. The duration-normalized indicators therefore provide the more appropriate comparison. These results are consistent with melt opportunity being the stronger diagnostic contrast between the two available Gangju La years. However, because only two observations are available, the analysis cannot establish whether thermal forcing was the dominant physical control or quantify the relative contribution of snowfall buffering.

The low snow fractions at Gangju La may also be relevant to the observed site behaviour. A lower snow fraction indicates that a larger share of total precipitation occurred as rainfall rather than snowfall in the ERA5-Land data. Rainfall does not provide the same surface-albedo benefit as snowfall and may coincide with warmer atmospheric conditions. Studies elsewhere in High Mountain Asia have shown that a declining snow ratio can weaken snow-albedo buffering and increase glacier sensitivity to warming (Liang et al., 2022). The Gangju La results are consistent with this general mechanism, although the reanalysis-derived snow fraction should be interpreted as a relative indicator rather than a locally validated precipitation-phase measurement.

The contrast between Thana and Gangju La should not be interpreted as a direct glacier-to-glacier comparison of absolute PWI values alone. The glaciers differ in area, elevation range, slope, aspect and local topographic setting. Gangju La is smaller, lower and steeper, while Thana is larger, higher and more gently sloping. These differences may influence radiation exposure, snow redistribution, accumulation patterns and the representativeness of the ERA5-Land grid cell. In particular, the approximately 9 km ERA5-Land grid is much larger than either glacier and is especially coarse relative to Gangju La. The higher post-snow PDD values at Gangju La may therefore reflect both genuine site-level climatic differences and limitations associated with representing a small glacier using a single grid cell. The comparison is most useful for identifying contrasting diagnostic regimes rather than claiming that glacier geometry alone explains the observed differences.

The k-sensitivity analysis provides an important test of whether the PWI interpretation depends on the selected decay parameter. The principal value of $k = 20$ °C·day was adapted from the e-folding thermal scale implied by the Brock-type snow-albedo ageing formulation applied in the Langtang catchment. However, this value was not calibrated specifically for Thana or Gangju La, and the present analysis uses daily mean temperature rather than the positive daily maximum temperature used in the original snow-albedo formulation. Evaluating k values from 5 to 80 °C·day was therefore necessary to determine whether the interpretation remained stable under different assumptions about how rapidly snowfall influence declines.

At Thana, the ordering of the years remains stable from k = 20 °C·day onward. This indicates that the main interannual interpretation is not sensitive to choosing k = 20, 40, 60 or 80 °C·day. The magnitude of PWI changes with k, but the relative ordering of 2024, 2023 and 2025 does not. At Gangju La, PWI remains low at small and moderate k values and increases mainly when slower decay is assumed. This behaviour is consistent with the high postPDD→Jun1 values at the site. The sensitivity analysis therefore shows that the two glaciers respond differently to the assumed persistence scale within the diagnostic framework.

The ratio R = PWI40/PWI20 provides a compact summary of the change between the reference and slower-decay cases. At Thana, R remains comparatively close to one, particularly in 2023 and 2025,indicating relatively limited change between the two persistence assumptions. At Gangju La, R is larger because PWI20 is very small. This ratio must be interpreted carefully, especially when the denominator approaches zero. A large R does not necessarily imply a proportionally large physical change in snowfall persistence; it may partly result from division by a very small PWI20 value. For this reason, the complete PWI values across the full k range provide a more reliable basis for interpretation than the ratio alone.

The separation of the survey windows into October–March, April–May and June–September is also important for interpreting the results. October–March captures the principal cold-season accumulation period, while June–September represents the primary monsoon and warm-season melt period. April–May forms a transition between these regimes and is the period during which snowfall may most directly influence the glacier surface entering the main melt season. Treating April–May separately therefore helps distinguish total seasonal accumulation from the timing of snowfall that may affect early-summer albedo conditions. This approach is particularly useful in the Bhutan Himalaya, where winter westerly snowfall and summer monsoon precipitation contribute differently to the annual hydroclimatic cycle.

Overall, the results demonstrate that PDD, snowfall amount, snow fraction and PWI provide complementary rather than competing information. PDD characterizes melt opportunity, snow fraction indicates precipitation-phase partitioning, total snowfall represents potential accumulation, and PWI emphasizes the timing of April–May snowfall relative to subsequent thermal exposure. At Thana, the combined indicators show a coherent interannual ordering from k = 20 °C·day onward. At Gangju La, the low PWI values and higher post-snow PDD indicate that thermal exposure may limit the potential influence of late-spring snowfall. The framework therefore provides a structured and reproducible way to interpret annual mass-balance variability when direct meteorological and surface-energy-balance observations are unavailable.

The principal contribution of the study is methodological rather than statistical. The short observation periods prevent correlation analysis, significance testing and formal attribution. Future application to the longer Thana and Gangju La records will require exact survey dates, consistently reported uncertainty and, ideally, local observations of air temperature, snowfall, snow-cover duration or surface albedo. Such data would allow the adapted persistence scale to be evaluated and potentially calibrated for Bhutanese glacier conditions. Until then, the PWI should be treated as a comparative diagnostic that supports, but does not replace, field observations and broader glacier-climate analysis.

**Limitations**

ERA5-Land represents grid-cell meteorological conditions and may not fully resolve microclimatic gradients over steep glacier terrain (Muñoz-Sabater et al., 2021). Reanalysis temperature and precipitation products can show elevation-dependent biases in complex Himalayan topography (Chen et al., 2021; Dorji et al., 2025), and diagnostics based on daily mean temperature can miss diurnal variability. The metrics are therefore interpreted as relative indicators of seasonal forcing and buffering, not as exact reconstructions of local surface energy fluxes. ERA5-Land biases are assumed to be temporally consistent across the short analysis windows, such that systematic offsets do not affect interannual comparisons within each site; non-stationary biases, while possible, are considered negligible over the 2–3-year periods analyzed. No formal significance testing is performed for the direct observation windows because n = 2-3 is insufficient for meaningful inference. Extending the analysis to older mass-balance years will require systematic archiving of exact field-survey start and end dates.

## Conclusions

This study demonstrates a reproducible ERA5-Land framework for interpreting short-period glacier mass-balance variability using PDD-based melt opportunity, snowfall amount, snow fraction and April–May snowfall timing. At Thana, the ordering of PWI from $k$=20 °C·day onward was consistent with the reported mass-balance point estimates: 2024 had the lowest PWI and the most negative balance, 2023 occupied an intermediate position, and 2025 had the highest PWI and the least negative balance. This rank-order agreement supports the diagnostic relevance of late-spring snowfall buffering, although the three-year record is insufficient to establish a statistically robust relationship.

At Gangju La, low snow fractions, high post-snow PDD and low PWI at small and moderate (k) values indicate limited potential April–May buffering within the proposed framework. Duration-normalized melt-opportunity indicators provide the clearer contrast between the two available years.

PWI is therefore best used as a complementary indicator rather than a standalone predictor. Its interpretation should be combined with PDD, snowfall amount, snow fraction, field-survey timing and glacier-specific conditions. Given the short observation period and the lack of local calibration of $k$, the findings represent a methodological case-study demonstration rather than statistically conclusive attribution of glacier mass-balance drivers.

## References


Bookhagen, B., & Burbank, D. W. (2010). Toward a complete Himalayan hydrological budget: Spatiotemporal distribution of snowmelt and rainfall and their impact on river discharge. Journal of Geophysical Research: Earth Surface, 115(F3),F03019. https://doi.org/10.1029/2009JF001426

Braithwaite, R. J., & Hughes, P. D. (2022). Positive degree-day sums in the Alps: A direct link between glacier melt and international climate policy. Journal of Glaciology, 68(271), 901–911. https://doi.org/10.1017/jog.2021.140.

Dorji, N., Awange, J. L., & Zerihun, A. (2025). Reliability of satellite, reanalysis and observation-based gridded temperature datasets for climate change impact studies in Bhutan. Science of Remote Sensing, 12, 100275. https://doi.org/10.1016/j.srs.2025.100275

Gurung, D. R., Kulkarni, A. V., Giriraj, A., Aung, K. S., & Shrestha, B. (2011b). Monitoring of seasonal snow cover in Bhutan using remote sensing technique. Current Science, 101(10), 1364–1370.

Hall, D. K., Riggs, G. A., Salomonson, V. V., DiGirolamo, N. E., & Bayr, K. J. (2022). MODIS/Terra Snow Cover 8-Day L3 Global 500m SIN Grid, Version 61 [Data set]. National Snow and Ice Data Center. https://doi.org/10.5067/MODIS/MOD10A2.061

Hersbach, H., Bell, B., Berrisford, P., et al. (2020). The ERA5 global reanalysis. Quarterly Journal of the Royal Meteorological Society, 146(730), 1999–2049. https://doi.org/10.1002/qj.3803

Hock, R. (2003). Temperature index melt modelling in mountain areas. Journal of Hydrology, 282(1–4), 104–115. https://doi.org/10.1016/S0022-1694(03)00257-9

Johnson, E., & Rupper, S. (2020). An examination of physical processes that trigger the albedo-feedback on glacier surfaces and implications for regional glacier mass balance across High MountainAsia. Frontiers in Earth Science, 8, 129.https://doi.org/10.3389/feart.2020.00129

Kumar, P., Saharwardi, M. S., Banerjee, A., Azam, M. F., Dubey, A. K., & Murtugudde, R. (2019). Snowfall variability dictates glacier mass balance variability in Himalaya-Karakoram. Scientific Reports, 9, 18192. https://doi.org/10.1038/s41598-019-54553-9

Liang, L., Cuo, L., & Liu, Q. (2022). The role of the snow ratio in mass balance change under a warming climate for the Dongkemadi Glacier, Tibetan Plateau. Journal of Climate, 35(12), 1–
30. https://doi.org/10.1175/JCLI-D-21-0762.1

Muñoz-Sabater, J., Dutra, E., Agustí-Panareda, A., Albergel, C., Arduini, G., Balsamo, G., Boussetta, S., Choulga, M., Harrigan, S., Hersbach, H., Martens, B., Miralles, D. G., Piles, M., Rodríguez-Fernández, N. J., Zsoter, E., Buontempo, C., & Thépaut, J.-N. (2021). ERA5-Land: A state-of-the-art global reanalysis dataset for land applications. *Earth System Science Data*, *13*, 4349–4383. https://doi.org/10.5194/essd-13-4349-2021

Nepal, J., Bhlon, R., Wang, L., Shrestha, M., Chen, D., Liu, H., Li, N., & Li, X. (2025). Quantifying the impact of snow drought on glacier melting at a Himalayan mountain basin. Journal of Hydrology, 661(Pt B), 133736. https://doi.org/10.1016/j.jhydrol.2025.133736

Ren, J., Jia, L., Miles, E. S., Menenti, M., Kneib, M., Shaw, T. E., & Buri, P. (2024). Observed and projected declines in glacier albedo across the Third Pole. One Earth, 7(9), 1587 - 1599 https://doi.org/10.1016/j.oneear.2024.08.010

NCHM (2025). The atmospheric dynamics and meteorological processes associated with the rare and historic snowfall of 2021–22 winter season in Bhutan. Bhutan HydroMet Journal, 4, 4–39.

Brock, B. W., Willis, I. C., & Sharp, M. J. (2000). Measurement and parameterization of albedo variations at Haut Glacier d'Arolla, Switzerland. Journal of Glaciology, 46(155), 675–688.

Sun, H., Su, F., Yao, T., He, Z., Tang, G., Huang, J., Zheng, B., Meng, F., Ou, T., & Chen, D. (2021). General overestimation of ERA5 precipitation in flow simulations for High Mountain Asia basins. *Environmental Research Communications*, *3*(12), 121003.

Stigter, E. E., Wanders, N., Saloranta, T. M., Shea, J. M., Bierkens, M. F. P., & Immerzeel, W. W. (2017). Assimilation of snow cover and snow depth into a snow model to estimate snow water equivalent and snowmelt runoff in a Himalayan catchment. *The Cryosphere, 11*, 1647–1664.

National Centre for Hydrology and Meteorology (NCHM). (2024). *Glacier mass balance studies on Gangju La Glacier 2023–2024*. Technical Report. Thimphu, Bhutan: NCHM.

National Centre for Hydrology and Meteorology (NCHM). (2024). *Glacier mass balance studies on Thana Glacier 2023–2024*. Technical Report. Thimphu, Bhutan: NCHM.

National Centre for Hydrology and Meteorology (NCHM). (2024). *State of the Climate Report 2024*. Thimphu, Bhutan: NCHM. This report includes the historical Gangju La and Thana mass-balance series, including the 2022–2023 values.

National Centre for Hydrology and Meteorology (NCHM). (2025). *Glacier mass balance studies on Gangju La Glacier 2024–2025*. Technical Report. Thimphu, Bhutan: NCHM.

## Climate Warming impacts on aircraft takeoff performance at a high elevation, runaway-limited airport: Paro International Airport.

*Ms. Ugyen Lhamo, Aviation Meteorological Section, Meteorological Services Division, NCHM, Correspondence: ulhamo@nchm.gov.bt*

### Abstract

Aircraft take-off performance at high-elevation, runway-limited airports is highly sensitive to atmospheric density, which is increasingly affected by rising temperatures. This study quantifies both historical density driven variability and the potential impacts of future warming on Airbus A319 takeoff performance at Paro International Airport, Bhutan. A simplified Newtonian force balance model was driven using high resolution Automatic Weather Observation System (AWOS) data for the period 2019–2025 during the June-September (JJAS) monsoon season. Daily maximum temperature and reconstructed pressure were used to compute air density and evaluate the resulting takeoff distance required (TODR) and runway-limited maximum takeoff mass (MTOM). Analysis of historical variability shows that present day summer operations already occur close to the runway-length constraint, with performance exceedances increasing rapidly for modest increases in operating mass. Trend analyses and distributional changes illustrated in the figures demonstrate the sensitivity of takeoff performance to density fluctuations. To assess potential future impacts, uniform warming perturbations of +1°C, +2 °C and +3 °C, consistent with downscaled CMIP6 projections for Bhutan, were applied to the observed record. These scenario experiments reveal a nonlinear increase in runway exceedance frequency, with approximately 49% of JJAS days exceeding the available runway length under +3 °C warming at an operating mass of 59t. Maintaining present A319 operations under such conditions would require an additional runway margin of approximately 60-70m to accommodate 95% of exceedance days, with extreme cases exceeding 100m. Warming induced reductions in MTOM correspond to mean passenger-equivalent payload losses of approximately 2.4, 4.7 and 7.0 passengers per departure under +1 °C, +2 °C and +3 °C warming, respectively. These findings demonstrate that even modest warming may substantially reduce operational margins at high-elevation, runway-limited airports and underscore the importance of incorporating climate considerations into long-term aviation planning and infrastructure adaptation.

## Introduction

Aero plane performance during takeoff and landing (the transition between the runway and standard departure and arrival paths, normally to or from a height of 10m above the surface) is directly impacted by lower atmospheric temperature, pressure and the wind vector components (Gratton et al. , 2020). Aircraft takeoff distance required (TODR) and maximum take off mass (MTOM) are critical parameters for safe and efficient aviation operations. Temperature, pressure and air density are linked through the equation of state, and changes in these parameters can alter aerodynamic lift, drag, thrust performance, stall speed, TODR and MTOM. Warmer temperatures or lower pressure reduce air density, requiring higher true airspeeds to generate sufficient lift, thereby increasing the TODR. This not only increases TODR but, for a fixed runway length, also reduces the permissible MTOM, leading to operational payload restrictions. Aircraft operating at high-elevation airports are particularly vulnerable to changes in atmospheric density because reduced air pressure and increased temperatures combine to increase density altitude. Density altitude is a key determinant of aircraft performance because it influences engine thrust, aerodynamic lift, and the acceleration available during take-off (Anderson, 2017; Filippone, 2006). Airports located in mountainous regions therefore operate with inherently smaller performance margins and are especially sensitive to additional warming. In South Asia, summer meteorological conditions are strongly controlled by the South Asian monsoon, which is characterized by elevated temperatures, high humidity and substantial variability in atmospheric circulation. Recent studies have shown that the Himalayan region is experiencing warming at rates exceeding the global average, with significant implications for regional climate and extreme temperature events (Krishnan et al., 2020). Downscaled CMIP6 projections further indicate a persistent warming signal across Bhutan under all future emission pathways (NCHM, 2024). Such changes are expected to increase density altitude during the summer season, potentially exacerbating performance limitations at high-elevation airports.

Previous studies have demonstrated that increasing temperatures can significantly affect aircraft performance through reductions in air density and available thrust. Coffel et al. (2017) first showed that warming could impose payload restrictions at major U.S. airports, while Zhou et al. (2018) reported reductions in take-off performance and climb capability across several international airports.Similar vulnerabilities have subsequently been identified at Greek airports (Gratton et al., 2020), Chinese airports (Wang et al., 2023), Thai airports (Kiettamrongsakul et al.,2023), European airports (Williams et al., 2025), and more recently across the Euro-Mediterranean region, where Gallardo et al. (2026) demonstrated that increasing high temperature extremes may lead to MTOM reductions of several tonnes and an increasing frequency of severe payload limitations.

Paro International Airport (PIA) has experienced an exponential increase in passenger movements from 65,439 in 2020 to 339,357 in 2024, while annual air cargo reached approximately 671t in 2024. (MoIT, 2024). This rapid increase in passengers and freight trafficplaces additional pressure on an already performance limited airport, reinforcing the need for a deeper understanding of how variations in the atmospheric density affect takeoff distance and payload capacity. Paro International Airport is located at an elevation of 2235m a.s.l. and operates a single 2265m runway. Operations are further constrained by visual approach procedures, surrounding high terrain, and density-altitude effects, particularly during the summer months. Despite growing interest in climate related aviation impacts, studies have largely focused on major lowland airports in North America, Europe and East Asia. Investigations addressing mountainous, runway-limited airports remain scarce, and no published studies currently exist for Bhutan. Consequently, the sensitivity of aircraft performance to climate driven density changes at high-elevation Himalayan airports remains poorly understood.

This study applies a Newtonian force balance takeoff model to available AWOS data from 2019-2025 to evaluate the sensitivity of TODR and MTOM to density variations at Paro International Airport (PIA). The model is configured for the Airbus A319 (A5-RGF) but is generalizable to other fixed wing aircraft. In addition to quantifying historical performance sensitivities, the paper evaluates future warming increments of +1 °C, +2 °C, and +3 °C to provide an initial assessment of how future temperature changes may influence takeoff performance under realistic climate driven increases in density altitude.

The present analysis focuses on quantifying the first-order sensitivity of performance to density changes alone. Consequently, the results should be interpreted as density driven performance sensitivities rather than complete operational performance forecasts.

It is beyond the scope of this study to analyse surface wind vector components, runway contamination state, or detailed aircraft configuration adjustments. To the best of the author's knowledge, this represents the first published assessment of climate related aircraft performance sensitivity at Paro International Airport and, more broadly, for Bhutan.

## Methodology

### Input Data: Temperature

The study used high temporal resolution Automatic Weather Observation (AWOS) data from Paro International Airport for the period of 2019 - 2025. These data are maintained and archived by the National Centre for Hydrology and Meteorology (NCHM). To identify the season of greatest thermodynamic constraint, a monthly mean temperature heat map for 2019–2025 was constructed (Figure 1). The one-second observations were aggregated to daily statistics to ensure consistency with performance modelling assumptions and to reduce high-frequency variability not relevant to takeoff distance calculations. The analysis is restricted to June-September (JJAS) monsoon season because this period exhibits the most extreme density altitude conditions and therefore poses the most operational limitations for takeoff.

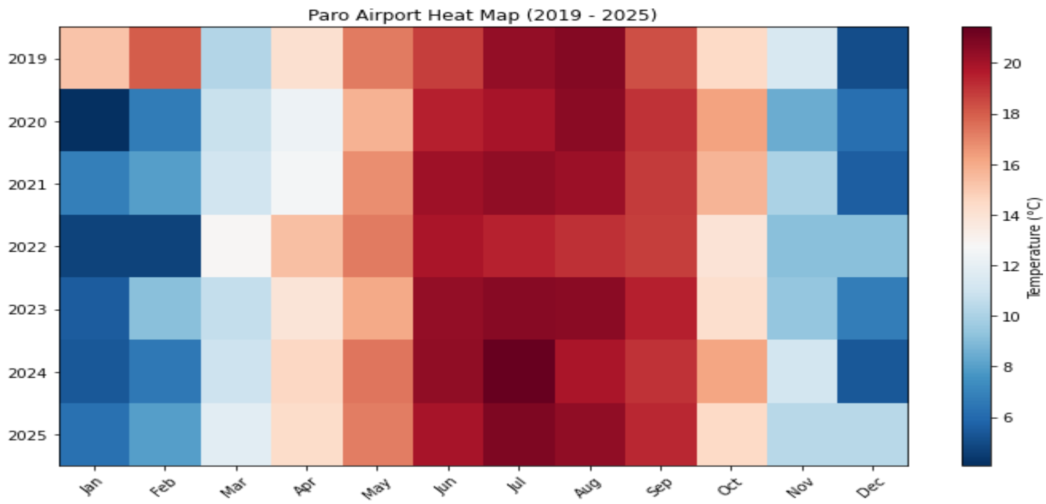


**Figure 1:** Monthly mean air temperature (°C) at Paro International Airport during 2019-2025 derived from AWOS observations. The heat map highlights the seasonal cycle of temperature and illustrates that the June–September (JJAS) period experiences the warmest conditions, corresponding to the most thermodynamically constrained period for aircraft take-off performance.

**Input Data: Pressure**

Due to corruption in the archived QFE (Atmospheric pressure at aerodrome elevation) data, station pressure was reconstructed from daily mean QNH (Altimeter setting referenced to mean sea level) and temperature using the standard ISA (International Standard Atmosphere) hypsometric relation. For each day $i$, QNH was redacted to QFE at runway elevation h = 2235m according to:

$$QFE_i = QNH_i\left(1 - \frac{Lh}{T_i + 273.15}\right)^{\frac{g}{R_d L}}$$

where $QFE_i$ is the daily mean pressure, $T_i$ is the daily mean air temperature, L = 0.0065 $K\ m^{-1}$ is the standard temperature lapse rate, g = 9.8 $ms^{-2}$ is the gravitational acceleration and $R_d$= 287.05 J $kg^{-1}\ K^{-1}$ is the gas constant for dry air. This produced daily QFE which was subsequently used to compute air density for the takeoff performance model. The hypsometric relation directly derives from the hydrostatic balance equation coupled with the ideal gas law, which together govern the vertical thermodynamic structure of the atmosphere under standard assumptions (Wallace & Hobbs, 2006; Holton & Hakim, 2013). Since QNH represents sea-level pressure adjusted using a standard atmospheric profile, conversion back to aerodrome level pressure via the inverse hypsometric formulation is physically consistent and routinely applied in aviation meteorology. The adoption of the ISA lapse rate introduces minor idealization, but the resulting pressure reconstruction remains internally consistent and accurate for evaluating seasonal density altitude sensitivity without introducing additional uncertainties.

**Air Density Computations**

Consistent with the methodology of Williams et al. (2025), daily air density for each JJAS day was calculated from reconstructed daily mean QFE pressure and daily maximum temperature using the ideal gas law (Wallace & Hobbs, 2006).

$$\rho_i = \frac{P_i}{R_d(T_i + 273.15)}$$

where $P_i$ is QFE (Pa), $T_i$ is the daily maximum temperature (∘C), and $R_d$= 287.05 J $kg^{-1}$ $K^{-1}$ is the gas constant for dry air. Although daily maximum temperature and daily mean pressure are not strictly simultaneous, diurnal pressure variations are relatively small compared with temperature fluctuations and are therefore expected to exert only a minor influence on the resulting density estimates. For the purpose of analyzing interannual variability in JJAS mean air density, the year 2022 was excluded because approximately two months of temperature observations were unavailable. Inclusion of an incomplete season would bias the seasonal mean, and no interpolation or infilling procedures were applied. This exclusion applies only to the density trend analysis presented in Figure 2; all subsequent TODR and MTOM calculations used all available observations. Accordingly, the omission of 2022 should be regarded as a data completeness issue rather than an indication of anomalous atmospheric conditions.

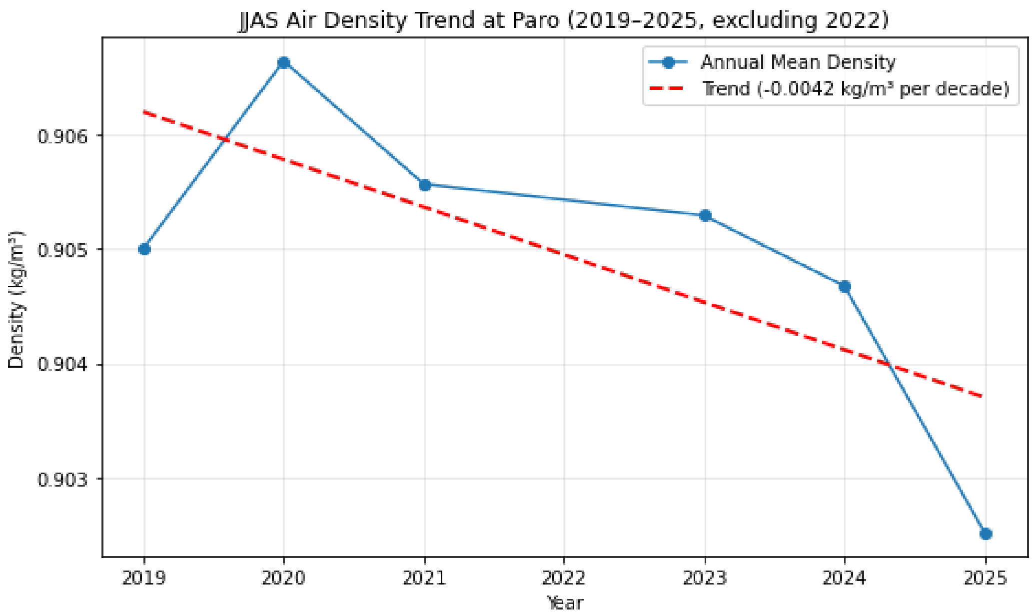


**Figure 2**: Interannual variability of JJAS mean air density at Paro International Airport during 2019-2025 derived from reconstructed pressure and daily maximum temperature. The year 2022 was excluded from the trend analysis because of incomplete observations. The dashed line denotes the least-squares linear fit and is included to illustrate interannual variability rather than to imply a statistically significant climate trend.

**Newtonian Force Balance model for TODR calculation**

A simplified Newtonian force balance model based on classical aircraft performance theory (Anderson, 2017) and adapted from the framework of Williams et al. (2025) was used to simulate the takeoff distance required (TODR) and the corresponding maximum takeoff mass (MTOM) for the Airbus A319. Figure 3 illustrates the forces and the geometric relationships considered in the computation of the TODR. Available engine thrust was assumed to scale linearly with air density according to

$$T(\rho) = T_{SL} \left(\frac{\rho}{\rho_0}\right)$$

where $\rho_0 = 1.225 kg\ m^{-3}$ is the ISA sea level density and $T_{SL}$ is the sea level static thrust. At each ground-roll speed V, the corresponding aerodynamic forces were evaluated from the dynamic pressure, from which lift and drag were calculated using representative aerodynamic coefficients. Rolling resistance was represented by a constant friction coefficient acting on the wheel load (W − L). The net acceleration was then obtained from Newton's second law

$$m\frac{dV}{dt} = T(\rho) - D(V,\rho) - \mu(W - L)$$

and the takeoff distance was then obtained by numerically integrating

$$ds = \frac{V}{a}\, dV$$

from an initial speed of 0.1 $m\ s^{-1}$ to the rotation speed: $V_R = 1.2\ V_s$, *where* $V_s$ denotes the 1-g stall speed. Following Williams et al. (2025), an additional 35ft (~10.7m) climb segment was incorporated to represent the conventional screen height used in aircraft performance calculations. Assuming a climb angle of approximately 7.7°, this corresponds to a horizontal distance of about 79m. A 15% safety factor was subsequently applied to account for operational variability and provide a conservative estimate of the total take-off distance required (TODR), yielding

$$TODR = 1.15\ (S_{ground} + 79m)$$

where $Sground$ denotes the computed ground roll distance.

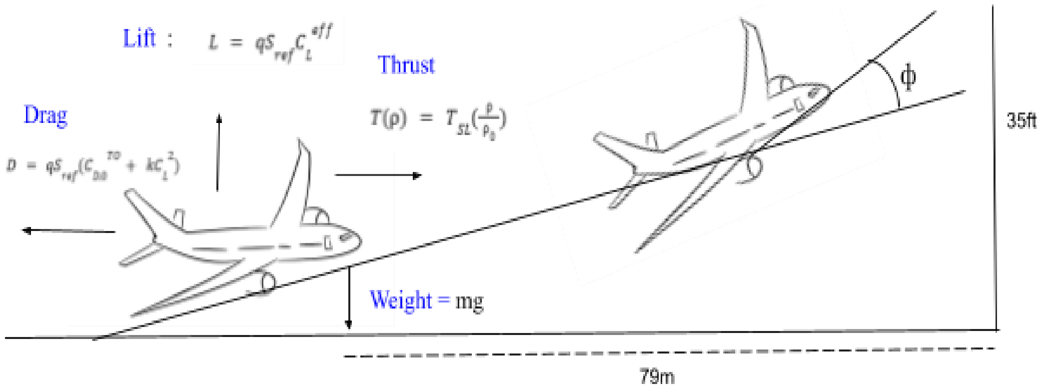


**Figure 3:** Schematic representation of the forces and geometric relationships considered in the simplified Newtonian force balance model used to compute the takeoff distance required (TODR). The diagram illustrates the principal forces acting during the ground roll, including thrust, drag, lift, weight and rolling resistance, together with the relevant speed and distance parameters used in the calculation.

For operational contexts, MTOM is often more relevant than TODR to determine what mass can be accommodated within a fixed runway length under different meteorological parameters. For agiven day $i$, with air density $\rho_i$, MTOM is defined as the biggest aircraft mass $M_{\max}$ such that the compouted TODR doesnot excxeed the available runaway length at PLA which is 2265m.

$$M_{max}(\rho i) = max\{ M : TODR\ (M, \rho i) \leq 2265\ m \}$$

Williams et al. (2025) achieved this inverse problem using a search algorithm that iteratively evaluates TODR at decreasing values of takeoff mass until the TODR is equal to the runway length, which is faster than the ‘brute force’ method by over an order of magnitude but they noted that alternative algorithms, such as binary search could potentially obtain the findings of the MTOM more efficiently. Following this recommendation, this study implements a binary search algorithm to determine MTOM for each day in the JJAS from 2019 to 2025. For each day,TODR was evaluated as a function of aircraft mass at the observed air density. Since TODR increases monotonically with mass, the maximum allowable take-off mass was determined by iteratively narrowing a bounded mass interval (40-70t) until the heaviest mass satisfying TODR ≤ 2265 m was identified. Convergence was achieved to within 1 kg.

Although the certified maximum takeoff mass of the Airbus A319 is 64t, routine JJAS operations at Paro are conducted at substantially lower masses owing to the combined effects of high elevation, runway-length limitations and elevated density altitude. Discussions with operating flight crews and performance calculations performed using onboard electronic flight bag systems indicate that practical summer operating masses typically range between 57 and 59t. Accordingly, 59t was adopted as a representative baseline operating mass for evaluating climate driven performance sensitivity.

Aircraft geometric and propulsion characteristics were obtained from Airbus Airport and Maintenance Planning documents (Airbus, 2023, 2024). The wing reference area (122.4 m²), engine configuration and sea-level static thrust correspond to the Airbus A319 equipped with CFM56-5B engines. Representative aerodynamic coefficients consistent with values commonly adopted in aircraft performance analyses (Anderson, 2017; Filippone, 2006) were employed. Since detailed manufacturer aerodynamic polars are proprietary, the selected coefficients are intended to capture first-order performance sensitivity rather than exact certification level performance.

**Warming Scenarios**

Climate change projections for Bhutan derived from downscaled CMIP6 simulations indicate that warming of approximately +1 °C is representative of near-term conditions (2021–2040) across most SSP pathways, while +2 °C is broadly consistent with mid-century warming under intermediate scenarios such as SSP2-4.5. Warming exceeding +3 °C is primarily associated with late century high-emissions scenarios, particularly SSP5-8.5 (NCHM,2024). Accordingly, uniform perturbations of +1°C, +2°C and +3°C were adopted as representative near-, mid- and late-century warming scenarios for western Bhutan. The resulting changes in TODR and MTOM should therefore be interpreted as first-order sensitivity estimates rather than operational forecast

## Discussions and Results

## Variability of takeoff performance during JJAS

The results demonstrate the daily variation in takeoff distance required (TODR) for the Airbus A319 (A5-RGF) at Paro International Airport during the JJAS months from 2019 to 2025, computed for three operating masses (57t, 59t and 60t). Based on pilot reported operational data, the typical maximum takeoff mass during JJAS is 57t to 59t for the Airbus A319. The higher mass of 60t is included to provide a comparative assessment of performance sensitivity beyond the current operational practice.

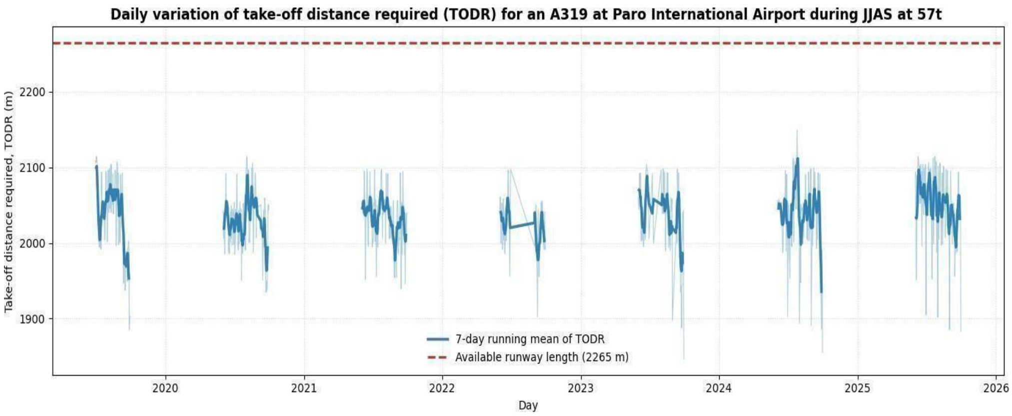


**Figure 4:** Daily variation of takeoff distance required (TODR) for the Airbus A319 at an operating mass of 57t during the JJAS seasons of 2019-2025. The horizontal dashed line indicates the available runway length of 2265m. Daily values and the corresponding 7-day running mean illustrate the variability in density driven performance under present climatic conditions.

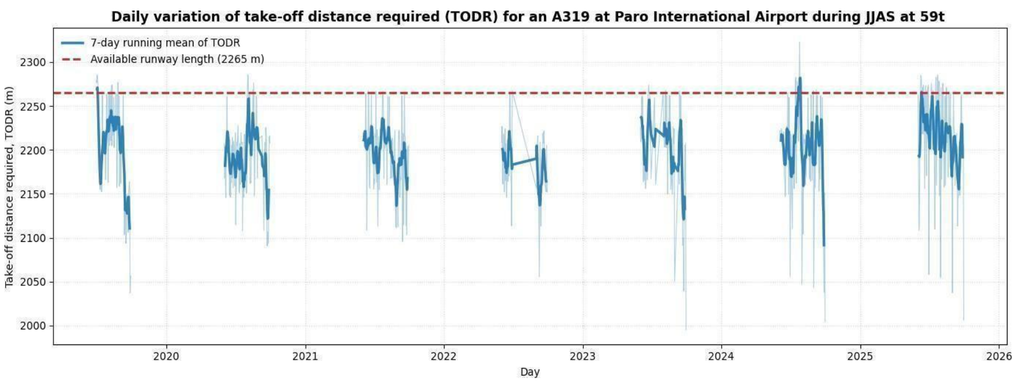


**Figure 5:** Daily variation of takeoff distance required (TODR) for the Airbus A319 at an operating mass of 59t during the JJAS seasons of 2019-2025. The horizontal dashed line indicates the available runway length of 2265m. Daily values and the corresponding 7-day running mean illustrate the variability in density driven performance under present climatic conditions.

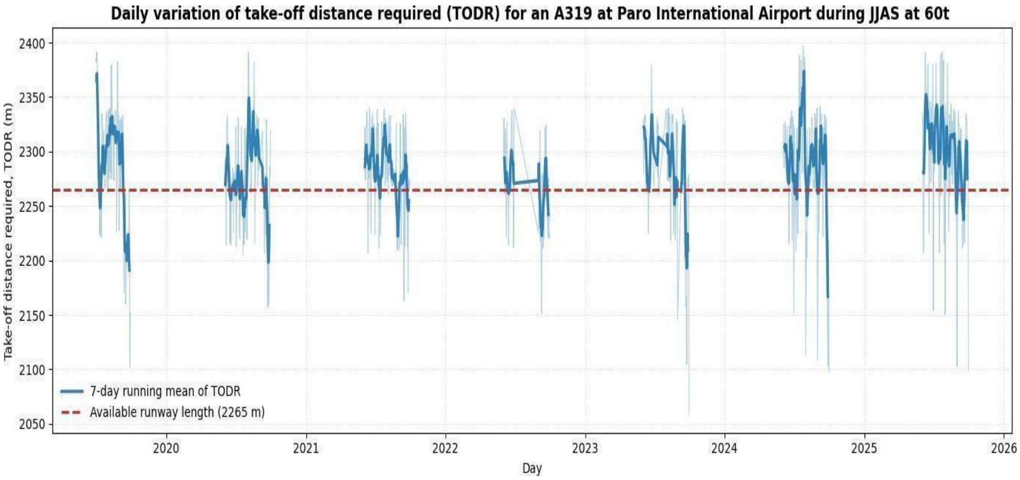


**Figure 6:** Daily variation of takeoff distance required (TODR) for the Airbus A319 at an operating mass of 60t during the JJAS seasons of 2019-2025. The horizontal dashed line indicates the available runway length of 2265m. Daily values and the corresponding 7-day running mean illustrate the variability in density driven performance under present climatic conditions.

At an operating mass of 57t, TODR remains below the available runway length of 2265m throughout all JJAS seasons analysed. While day-to-day variability is evident, neither the daily values nor the 7-day running mean exceed the operational limit, indicating that present day summer operations at Paro are generally feasible at this mass. However, the proximity of TODR to the runway constraint highlights that routine operations occur with limited performance margin, leaving little tolerance for adverse meteorological conditions or additional loading. At an operating mass of 59t, which remains well below the certified MTOM, TODR exceedances of the available runway length occur on approximately 10.94% of JJAS days. This indicates that even a modest increase in operating mass beyond current practice could lead to frequent performance constraints. At 60t, runway-length exceedances became dominant, occurring on 75.57% of JJAS days, making operations challenging during the summer months without substantial payload restrictions or favourable wind conditions. These results show that density driven effects alone are sufficient to impose operational limitations during the monsoon season, even when operating well below the aircraft's certified takeoff mass.

### Trends in mean takeoff distance and maximum takeoff mass

Figure 7 illustrates the interannual variability of JJAS-mean TODR and MTOM derived from the Newtonian force balance model for the period 2019-2025 (excluding 2022 because of incomplete observations). The JJAS-mean TODR increases by approximately 20.7 m decade$^{-1}$, while the corresponding JJAS-mean MTOM decreases by approximately 0.27 t decade$^{-1}$, consistent with the observed reduction in JJAS-mean air density. Given the limited observational record comprising only six complete JJAS seasons, the fitted trends are intended to illustrate the sensitivity of aircraft performance to interannual density fluctuations rather than to represent statistically robust climate change signals.

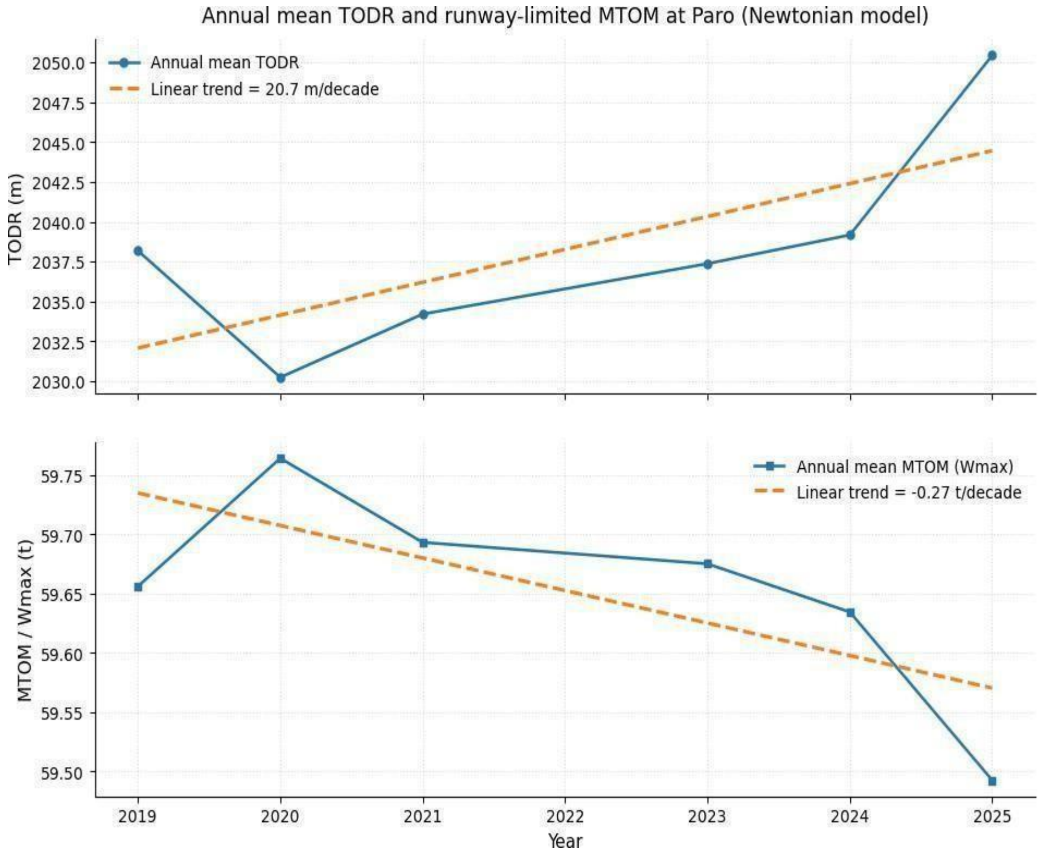

**Figure 7:** Interannual variability of JJAS-mean takeoff distance required (TODR) and runway-limited maximum takeoff mass (MTOM) at Paro International Airport during 2019-2025 (excluding 2022 because of incomplete observations), derived from the Newtonian force balance model. Dashed lines represent least-squares linear fits and are shown to illustrate interannual variability rather than statistically robust climate trends.

**Distributional changes in the take off performance under warming scenarios**

To quantify the effects of warming temperatures, the JJAS distribution of TODR was evaluated at an operating mass of 59t under baseline conditions and under uniform temperature perturbations of +1 °C, +2 °C, and +3 °C. These scenarios are selected to align with downscaled CMIP6 projections for the Paro region, representing near, mid and late century JJAS warming across a range of emissions pathways. Under baseline conditions, the TODR distribution remains confined below the available runway length of 2265m, indicating that present summer operations are feasible with a limited operating mass of 59t. The introduction of a +1 °C warming results in a systematic rightward shift of the TODR distribution, leading to exceedance of the runway-length by approximately 22.6% of JJAS days (Figure 8). Under +2 °C warming the runway exceedance increases to approximately 35.8% (Figure 9), while under
+3 °C warming, approximately 49% of JJAS days (Figure 10)

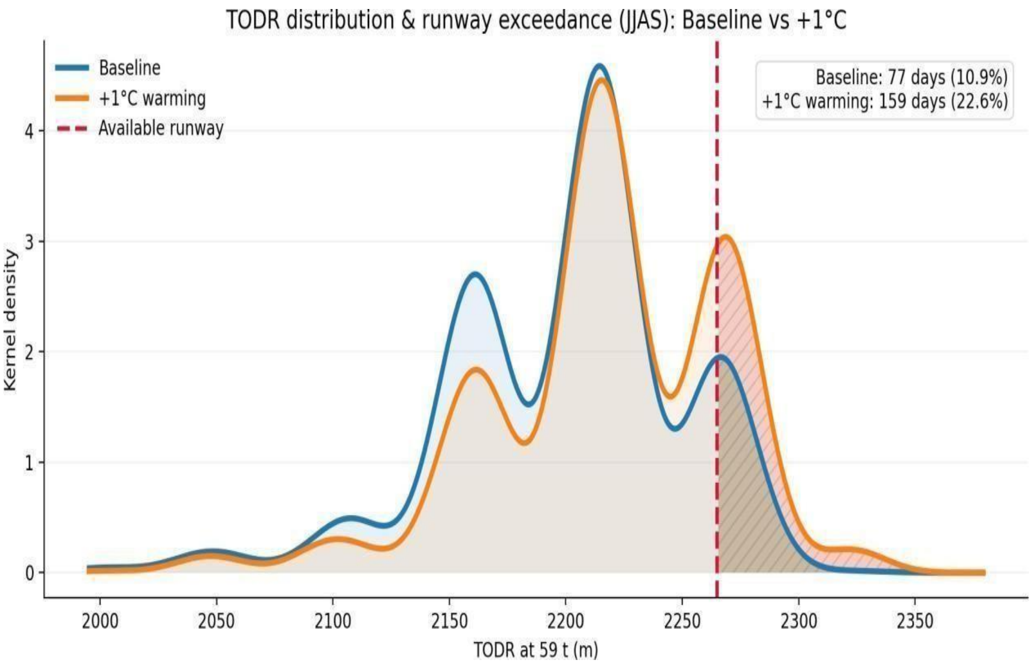


.

**Figure 8:** Probability distribution of JJAS takeoff distance required (TODR) for a 59t Airbus A319 under baseline conditions and under a uniform +1 °C warming perturbation. The vertical dashed line indicates the available runway length of 2265m. Shaded areas beyond the runway limit correspond to exceedance conditions.

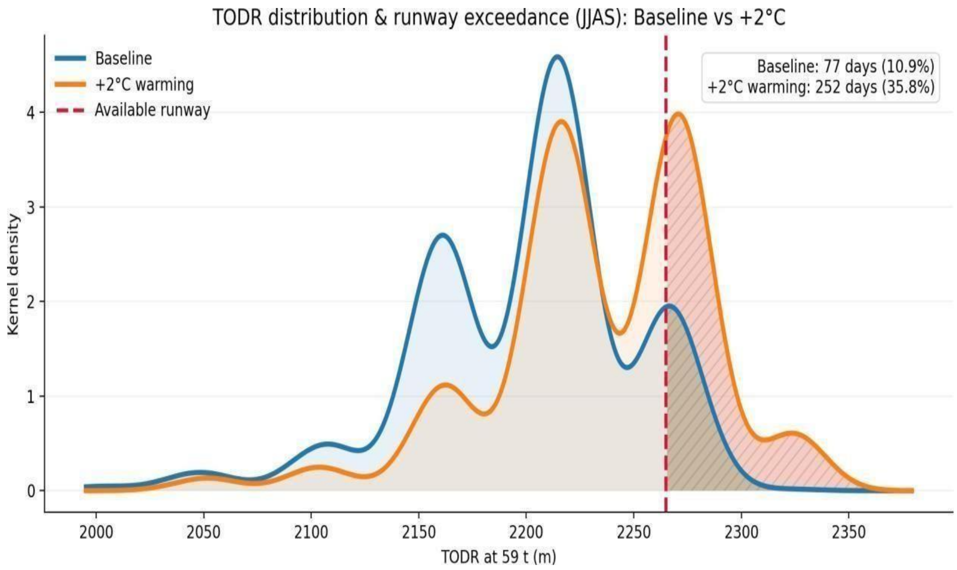


**Figure 9:** Probability distribution of JJAS takeoff distance required (TODR) for a 59t Airbus A319 under baseline conditions and under a uniform +2 °C warming perturbation. The vertical dashed line indicates the available runway length of 2265m. Shaded areas beyond the runway limit correspond to exceedance conditions.

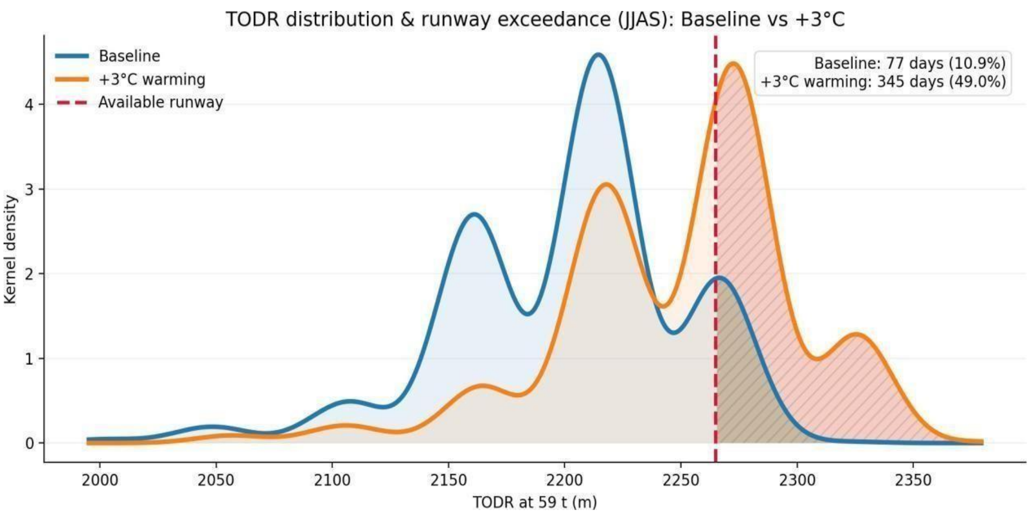


**Figure 10**: Probability distribution of JJAS takeoff distance required (TODR) for a 59t Airbus A319 under baseline conditions and under a uniform +3 °C warming perturbation. The vertical dashed line indicates the available runway length of 2265m. Shaded areas beyond the runway limit correspond to exceedance conditions.

The increase in runway exceedance under progressive warming scenarios exhibits a distinctly nonlinear response, due to two interacting physical and operational mechanisms. First, jet engine thrust is approximately proportional to air density, such that warming induced reductions in density directly decrease the available thrust during the takeoff and thereby reducing the net propulsive force. Since acceleration is determined by the balance between thrust, aerodynamic drag, rolling resistance and aircraft weight, even a slight decrease in thrust can lead to significant decrease in acceleration. Take off distance is inversely proportional to acceleration and therefore a small decrease in acceleration can disproportionately increase the required ground roll distance. This introduces a nonlinear sensitivity of TODR to incremental density changes.

Second, exceedance is not only governed by distance changes alone but also by comparison against a fixed available runway length. As the entire distribution of TODR shifts toward higher values under uniform warming perturbations, days that were previously near the operational margin transition into exceedance conditions. This amplifies the upper tail of the distribution and once operations approach the runway limit, increasing thermodynamic perturbations produce a rapid increase in the number of days exceeding runway limit. The practical implication is that performance limiting days do not increase linearly with temperature but instead expand rapidly once the operational envelope approaches its physical limit. In such conditions, maintaining the current operational levels would require either payload restrictions, increased dependence on favorable wind components or infrastructure adaptation.

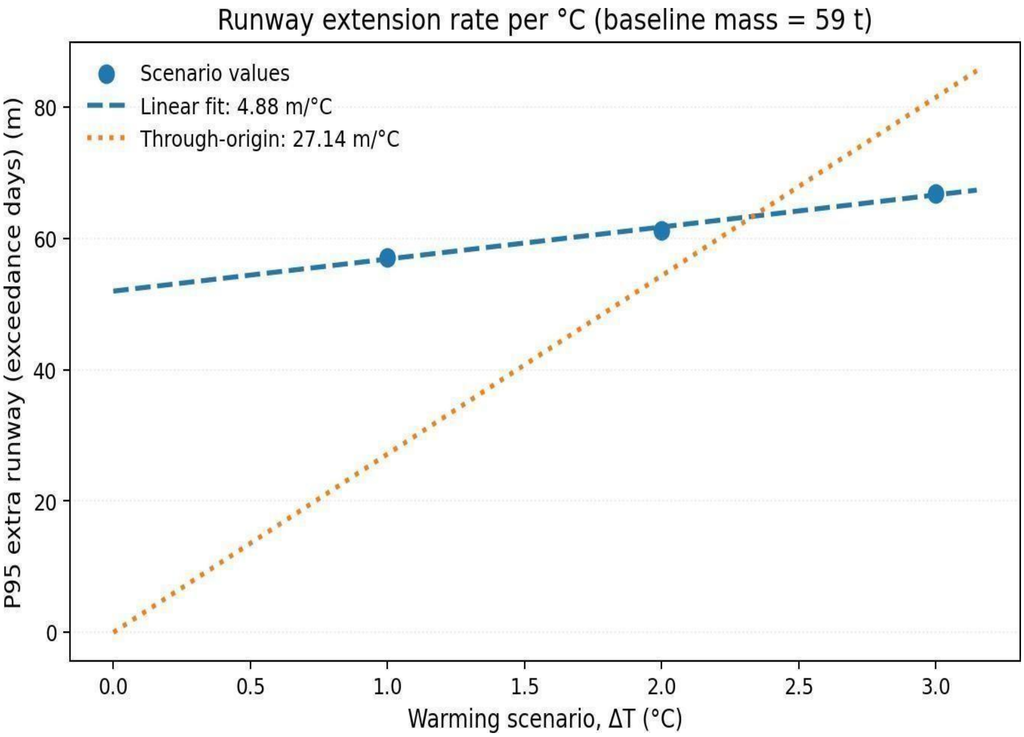


**Figure 11:** Additional runway length required under incremental warming scenarios for a baseline operating mass of 59t. The values represent the runway extension needed to accommodate 95% of JJAS departures and illustrate the potential infrastructure adaptation required to maintain present day Airbus A319 operations at Paro International Airport.

Figure 11 quantifies the additional runway length required under incremental warming, expressed as the additional runway length necessary to reduce exceedances to the 95th percentile (P95) of JJAS days at a baseline operating mass of 59t. The runway extension analysis is intended as an illustrative adaptation metric rather than an engineering design recommendation. A 95th percentile criterion was adopted so that the required runway length would accommodate at least 95% of JJAS operating days, thereby limiting performance exceedances to fewer than 5% of seasonal departures. For each warming scenario, the available runway length was progressively increased until the fraction of exceedance days fell below this threshold. The required runway extension increases approximately linearly with warming. Under the +3 °C scenario, an additional runway length of approximately 60-70 m would be required to accommodate 95% of JJAS departures, while extreme conditions may require more than 100m.

**Implications for MTOM and payload capacity**

Operational decision making in aviation is governed primarily by the allowable takeoff mass under fixed runway-length constraints. To quantify the implications of warming to represent an operationally intuitive metric, i.e transport capacity, the runway-limited maximum takeoff mass (MTOM) was evaluated for each JJAS day under baseline conditions and under uniform warming perturbations of +1 °C, +2 °C, and +3 °C, assuming a fixed runway length of 2265m. Figure 12 illustrates the resulting distribution of passenger-equivalent payload loss per takeoff during the JJAS season under these warming scenarios. Payload loss is derived from the MTOM analysis and expressed as an equivalent number of passengers by assuming an average mass of 84 kg per passenger, inclusive of baggage, consistent with EASA guidance.

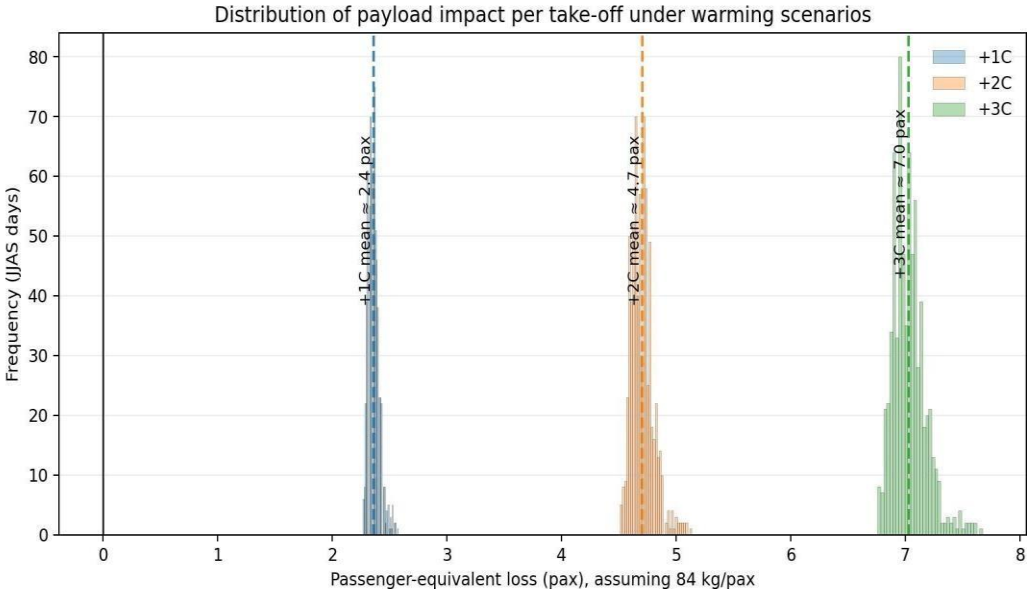


**Figure 12:** Distribution of passenger-equivalent payload losses per departure under +1°C, +2°C and +3°C warming scenarios, derived from reductions in maximum takeoff mass. Passenger equivalents assume an average mass of 84 kg including baggage.

Under a +1°C warming scenario, the distribution of passenger-equivalent payload loss is approximately 2.4 passengers per departure. Under +2°C warming, the distribution shifts further rightward, with a mean payload loss of approximately 4.7 passengers per departure. Under the +3°C warming scenario, the distribution exhibits a pronounced rightward shift, with a mean payload loss of approximately 7.0 passengers per departure and a substantially wider dispersion. The widening of the distribution with increasing warming reflects the compounding influence of density driven performance degradation during already extreme summer conditions. To illustrate the cumulative seasonal implications of per flight payload penalties, a representative value of five departures per day was adopted based on present day A319 operations at Paro International Airport. This assumption is used solely to provide an order-of-magnitude estimate of seasonal transport impacts and should not be interpreted as a forecast of future traffic demand. A mean passenger-equivalent payload loss of approximately 2.4 passengers per departure under +1°C warming corresponds to accumulative seasonal reduction of roughly 1,464 passengers. Under +2°C warming, the estimated seasonal loss increases to approximately 2,867 passengers, while under +3°C warming, cumulative losses approach 4,270 passengers over the summer season. These values are not intended as precise forecasts and will depend on actual traffic volumes, aircraft scheduling and operational practices. Rather, they are presented to illustrate how relatively modest payload penalties at the individual flight level can accumulate into substantial reductions in seasonal transport capacity.

The progression from +1°C to +3°C warming demonstrates a near linear increase in mean passenger-equivalent payload loss, but a markedly nonlinear increase in the variability and upper-tail severity of payload restrictions. This behavior is consistent with the distributional shifts in takeoff distance and runway exceedance risk discussed and highlights that warming affects not only average payload capacity but also the predictability and reliability of operations.

## Conclusions

This study demonstrates that takeoff performance at Paro International Airport is already strongly constrained by atmospheric density during the JJAS monsoon season, and that even modest warming has the potential to substantially degrade operational margins. Using a Newtonian force balance model driven by high-resolution observational data, the study shows that present day summer operations for the Airbus A319 occur close to the runway-length limit at realistic operating masses, leaving little tolerance for adverse meteorological conditions or additional loading. Scenario experiments aligned with CMIP6-based warming projections indicate that mean takeoff distance and runway-limited maximum takeoff mass change approximately linearly with increasing temperature. In contrast, the frequency and severity of performance-limiting conditions increase nonlinearly owing to shifts in the upper tail of the takeoff distance distribution. When expressed in operationally meaningful terms, warming induced reductions in allowable take-off mass translate into recurring payload penalties equivalent to several passengers per departure.

While this study focuses on a single aircraft type and excludes wind effects, the framework is general and readily extendable to other aircraft and additional meteorological factors. Several limitations should be acknowledged. The analysis employs a simplified force balance framework and considers only density driven effects, while wind components, runway contamination, aircraft configuration changes and detailed engine characteristics were not explicitly represented. Furthermore, the warming scenarios represent idealized perturbations and should not be interpreted as operational forecasts. Despite these limitations, the results consistently demonstrate that continued warming is likely to reduce operational margins at high-elevation, runway-limited airports and highlight the importance of integrating climate sensitivity into aviation planning and long-term adaptation strategies.

**Appendix A**: Model parameters used in the Newtonian force balance calculations

| Parameter | Symbol | Value | Units | Notes |
|---|---|---|---|---|
| Gravitational acceleration | g | 9.80665 | m s^-2 | Standard gravity |
| ISA sea-level density | rho0 | 1.225 | kg m^-3 | Reference density |
| Wing reference area (A319) | S | 122.4 | m^2 | Airbus (2023) |
| Sea-level static thrust per engine | T_SL,eng | 108400 | N | CFM56-5B7/P rating |
| Number of engines | n | 2 | - | Twin-engine |
| Total sea-level thrust | T_SL | 216800 | N | n × T_SL,eng |
| Max lift coefficient (TO config) | CL_max | 2.0 | - | Anderson (2017) |
| Effective lift coefficient (ground roll) | CL_eff | 1.6 | - | 0.8 × CL_max |
| Zero-lift drag coefficient (TO config) | CD0 | 0.04 | - | (Filippone,2006) |
| Induced drag factor | k | 0.045 | - | (Filippone,2006) |
| Rolling friction coefficient | mu | 0.02 | - | Dry paved runway |
| Runway length (Paro) | L_RWY | 2265 | m | (MoIT,2024) |
| Rotation speed margin | VR/Vs | 1.2 | - | VR = 1.2 Vs |
| Integration step | dV | 0.5 | m s^-1 | Speed increment |
| 35-ft screen distance | s_35 | 79 | m | Williams et al. (2025) |
| Safety margin factor | - | 1.15 | - | Applied to total distance |

## References

Airbus. (2023). *Aircraft characteristics: Airport and maintenance planning—A319*. Airbus.

Airbus. (2024). *Aircraft characteristics: Airport and maintenance planning—A320 family* (Rev. Jun 01/24). Airbus.

Anderson, J. D. (2017). *Introduction to flight* (8th ed.). McGraw-Hill Education.

Coffel, E. D., Thompson, T. R., & Horton, R. M. (2017). The impacts of rising temperatures on aircraft takeoff performance. *Climatic Change,144,*381–388. https://doi.org/10.1007/s10584-017-2015-6

European Union Aviation Safety Agency. (2022). *Acceptable means of compliance (AMC) and guidance material (GM) to Part-CAT—CAT.OP.MPA.100 mass and balance*.

Filippone, A. (2006). *Flight performance of fixed and rotary wing aircraft*. Butterworth-Heinemann.

Gallardo, V., Sánchez-Gómez, E., Riber, E., Bonnet, S., & Jiménez-Guerrero, P. (2026). Assessing climate change impacts on aircraft takeoff performance: Potential consequences of increasing high-temperature extremes at Euro-Mediterranean airports.*Climatic Change, 179*, 46. https://doi.org/10.1007/s10584-026-04105-8

Gratton, G., Padhra, A., Rapsomanikis, S., Jones, B., & de León, R. R. (2020). The impacts of climate change on Greek airports. *Climatic Change*, *160*, 219–231. https://doi.org/10.1007/s10584-019-02634-z

Holton, J. R., & Hakim, G. J. (2013). *An introduction to dynamic meteorology* (5th ed.). Academic Press.

International Civil Aviation Organization. (2018). *Annex 3—Meteorological service for international air navigation* (20th ed.).

Kiettamrongsakul, P., Klongnava, N., & Amornmorakot, S. (2023). The impact of climate variability on aircraft take-off performance at Mae Fah Luang International Airport. In *Proceedings of the 3rd National Aviation Symposium* (pp. 44–61). https://proceedings.catc.or.th/proceeding/wp-content/uploads/2023/09/05-The-Impact-of-Climate-Variability-on-Aircraft-Take-off-Performance-at-Mae-Fah-Luang-International-Airport-page-44-61.pdf

Krishnan, R., Sanjay, J., Gnanaseelan, C., Mujumdar, M., Kulkarni, A., & Chakraborty, S. (Eds.). (2020). *Assessment of climate change over the Indian region*. Springer. https://link.springer.com/book/10.1007/978-981-15-4327-2

Ministry of Infrastructure and Transport. (2024). *Annual information bulletin 2024*. Royal Government of Bhutan. https://www.moit.gov.bt/wp-content/uploads/2025/06/Annual-information-bulletin-2024.pdf

National Centre for Hydrology and Meteorology. (2024). *Climate change projection report of Bhutan: Insights from CMIP6 projections*. Royal Government of Bhutan.

Wang, K., Peng, X., Dan, B., Zhang, Y., & Li, X. (2023). Decreased aircraft takeoff performance under global warming. *Atmosphere, 14*(1), 106. https://doi.org/10.3390/atmos14010106

Wallace, J. M., & Hobbs, P. V. (2006). *Atmospheric science: An introductory survey* (2nd ed.).Elsevier Academic Press.

Williams, J., Williams, P. D., Guerrini, F., & Venturini, M. (2025). Quantifying the effects of climate change on aircraft take-off performance at Europeanairports. *Aerospace*,*12*(3),165. https://doi.org/10.3390/aerospace12030165

Zhou, Y., Zhang, N., Li, C., Liu, Y., & Huang, P. (2018). Decreased takeoff performance of aircraft due to climate change. *Climatic Change, 151*(3), 463–472. https://doi.org/10.1007/s10584-018-2335-7

National Centre for Hydrology and Meteorology
Thimphu, Bhutan
Tel.No: +975-2- 327202
www.nchm.gov.bt